Chaos
An Interdisciplinary Journal of Nonlinear Science

RESEARCH ARTICLE | AUGUST 14 2025

# Using unstable periodic orbits to understand blocking behavior in a low order land–atmosphere model

Oisín Hamilton ; Jonathan Demaeyer ; Michel Crucifix ; Stéphane Vannitsem



*Chaos* 35, 083126 (2025)
https://doi.org/10.1063/5.0268852

# Using unstable periodic orbits to understand blocking behavior in a low order land–atmosphere model

Cite as: Chaos 35, 083126 (2025); doi: 10.1063/5.0268852
Submitted: 4 March 2025 · Accepted: 16 July 2025 ·
Published Online: 14 August 2025

View Online Export Citation CrossMark

Oisín Hamilton,[1,2,a] Jonathan Demaeyer,[1] Michel Crucifix,[2] and Stéphane Vannitsem[1]

## AFFILIATIONS

[1]Royal Meteorological Institute of Belgium, Brussels, Belgium
[2]UCLouvain—Earth and Life Institute, Louvain la Neuve, Belgium

[a)]**Author to whom correspondence should be addressed:** oisin.hamilton@meteo.be

## ABSTRACT

Unstable Periodic Orbits (UPOs) were used to identify regimes, and transitions between regimes, in a reduced-order coupled atmosphere-land spectral model. In this paper, we describe how the chaotic attractor of this model was clustered using the numerically derived set of UPOs. Using continuation software, the origin of these clusters was also investigated. The flow of model trajectories can be approximated using UPOs, a concept known as shadowing. Here, we extend that idea to look at the number of times a UPO shadows a model trajectory over a fixed time period, which we call cumulative shadowing. This concept was used to identify sets of UPOs that describe different life cycles of each cluster. The different regions of the attractor that were identified in the current work, and the transitions between these regions, are linked to specific atmospheric features known as atmospheric blocks.



**Atmospheric blocking describes particular weather patterns that can cause prolonged extreme weather, such as heat waves or cold spells, in the midlatitudes. Currently, the physical mechanisms behind atmospheric blocking are not fully understood. In this paper, we study atmospheric blocking events—specifically their onset and decay—using a simple climate model. Such models can play a useful role in identifying the key physical behaviors that lead to blocking. In this model, specific regimes in phase space correspond to different atmospheric blocking conditions. We focus on solutions of the system that can explain why these regimes exist in the chaotic attractor. These solutions are known as unstable periodic orbits (UPOs), which are densely distributed in the chaotic attractor. This means that any trajectory is finitely close to a UPO at any given time. UPOs, therefore, provide a means of describing properties of the attractor and, by extension, the model climate. In this paper, we use UPOs to classify the regimes in the model climate and to identify the transitions between them. We then link these regimes and transitions to specific blocking patterns in the model, showing that persistent visits of the trajectory to regions of phase space associated with blocking events occur through well-defined channels. The resulting behavior in the model climate indicates that the onset and decay of persistent blocks produce predictable weather patterns. We also show that UPOs can serve as a simple early warning indicator for the onset and decay of such persistent blocking events.**

## I. INTRODUCTION

The atmosphere, while characterized by chaotic behavior, can exhibit some level of repetition over time spans of weeks or months.[1] This quasi-repeating behavior is called Low Frequency Variability (LFV). One example of LFV is midlatitude atmospheric blocking (from here referred to as blocks or blocking). Blocking causes the jet stream to be deflected, and in the midlatitudes, this deflects the eastward moving low pressure systems, while the area in the trough of the deflection experiences persistent weather.[2] This usually leads to heat waves and cold snaps in the midlatitudes. Heat waves are responsible for tens of thousands of excess deaths across the midlatitudes,[3,4] and numerical weather prediction methods still struggle with predicting the onset and decay of such events.[5] This is believed to be caused by missing subgrid processes and regional specific features, but there is still no clear consensus on the exact key physical processes that cause blocking.[6–8]

Climate change will increase the intensity, frequency, and duration of heat waves.[9] However, it is not clear what the impact of climate change will be on blocking events.[5,8,10,11] This is due to the lack of a comprehensive theory of blocking[12] and because climate change is expected to alter the magnitude of baroclinic instability at different levels of the atmosphere,[13] resulting in opposing influences on the atmospheric circulation.[14,15] Therefore, to fully understand the nature of blocking, it should also be studied from a conceptual point of view.

One way to tackle this problem conceptually is to use reduced order models to look at new approaches to describe and predict the dynamical properties of the atmosphere. This is the core concept of "bottom-up" analysis, which tries to identify fundamental dynamical mechanisms from fluid mechanics, thermodynamics, and dynamical system theory. Low-order models build upon a minimal set of key physical ingredients believed to be at the origin of the mechanisms of interest. They can, therefore, act as a testing ground to investigate new concepts for understanding and predicting LFV (see, e.g., Vautard and Legras,[16] Mak,[17] Nauw and Dijkstra,[18] Vannitsem *et al.*,[19] and Vannitsem *et al.*[20]). These models provide a cheap and flexible platform upon which to test concepts and can be simple enough to understand the underlying dynamics, which produce the climatological behavior. Once such behavior is understood, the aim is to then test whether similar behavior exists in more complex models and whether the same dynamical processes are present. Thus, this helps isolate and understand the key dynamical processes in the governing equations.[21,22]

Consistent with this strategy, we aim to study the onset and decay of blockings from a dynamical systems perspective by using the `qgs` (quasi-geostrophic spectral) model framework,[23] which we describe below. Our objective is to link features of the state space of the attractor, to the climatology of the model, with the aim of then describing the atmospheric behavior that we see from the dynamics of the model.

Weather regimes and LFV have been studied from a dynamical systems perspective in low order models since the early days of numerical weather prediction.[24,25] However, caution needs to be taken when interpreting results from low order models. On top of the obvious fact that these models only reproduce select behavior of the real atmosphere, they can also be highly susceptible to which wave modes (or model resolution) are included. This means that the resulting chaotic attractor, and in turn repeating behavior in the attractor, can differ wildly.[26] Convergence of the structure of the attractor with model resolution should, therefore, be checked.[27]

Work on reduced order models led to the hypothesis that persistent weather phenomena, and different weather regimes, could be explained by proximity of the trajectory to different fixed points with differing stability properties.[28–30] These fixed points correspond to different weather regimes, and as the trajectory is attracted to particular fixed points, the trajectory may remain in these regimes for some time before the unstable manifold repels the trajectory, and it continues its path on the chaotic attractor. The idea has since been expanded to look at areas of periodically repeating behavior,[31] and other regions of quasi-stationary, or very slowly altering behavior.[6] Our aim is to better understand how trajectories evolve through these systems, and how parameter changes will alter the chaotic attractor. These questions can be addressed using periodic orbit theory, which considers the periodic orbits of a dynamical system as building blocks of its attractor, helping to construct a skeleton of the dynamics.[32]

It was conjectured by Poincaré in the 19th century that chaotic systems could be approximated by periodic motions that are densely distributed within the attractor.[33] Unstable Periodic Orbits (UPOs) are closed loops in state space that provide a kind of topological invariant characterization of the attractor.[34] This means that they preserve topological relations between periodic orbits, such as their relative inter-windings, allowing for at least a partial organization of the state space. The use of these orbits to investigate the state space has since been called periodic orbit theory[32] and has been used in a wide range of fields to help describe properties of the attractor,[35–37] in particular, in the study of turbulent flows.[38–43]

Though numerically finding all of the UPOs in the chaotic attractor of a system is impossible, as they form a dense set, it has been found that usually a limited number of them—likely of low period[44,45]—can be used to describe the predominant behavior of the system. In simple systems, Maiocchi *et al.*[46] found that UPOs could help predict transitions between wings of the Lorenz 1963 attractor, among other important stability properties of the attractor. This work was expanded to the Lorenz 96 model in Maiocchi *et al.*,[47] where the authors suggest that Lyapunov analysis should be complimented with the use of UPOs to provide a global picture of the attractor.

UPOs have also been used in reduced order models of the climate. Using a barotropic ocean model, Kazantsev[31] found that, even with only a few low order UPOs, some key properties of the attractor, such as the PDF of model trajectories, could be predicted. This work was built on by Selten and Branstator,[48] using the Lorenz 84 model, who found that particular transition paths exist between weather regimes, and they hypothesize that the cycle seen in the weather patterns corresponds to a particular periodic orbit. Later, Gritsun,[49] using a more realistic barotropic atmosphere model, found that the most common paths of trajectories could also be explained in terms of particular orbits.

Kazantsev[50] investigated the impact of forcing on the model by analyzing the impact of the forcing on a small set of UPOs (∼20–30). This method allowed them to find the magnitude of forcing that caused the largest change in the averaged dynamics, allowing them to identify which forcings would have the largest impact on the climate of the model. Gritsun,[51] using a barotropic atmosphere model, attempted to use UPOs to calculate the response of the system to small external forcings. They concluded that the method could be utilized for understanding local sensitivity on specific orbits but likely cannot be used to understand the global behavior. This is a result of the computational cost in finding the UPOs, and the fact that it is impossible to know in more complex systems if all UPOs up to a period of $T$ have been found.

Lucarini and Gritsun[52] extended the approach of using UPOs to structure the state space in an intermediate complexity model. They found that blockings occur when the model trajectory is in the neighborhood of a particular set of UPOs, and that these UPOs generally have higher instability compared to the set of UPOs that describe zonal flows. This result could explain the local instability associated with blocking events. However, these promising results from periodic orbit theory become challenging to use in high

Lyapunov dimensional systems (or the Kaplan–Yorke dimension).[37] Therefore, the requirement for the orbits to be closed has been relaxed in some studies and extended to quasi-recurrent patterns in the attractor.[6]

In this paper, we use UPOs to provide an explanation to the structure of the chaotic attractor of a reduced-order land–atmosphere model and explain the persistence seen in different parts of the attractor. We use the UPOs to also define transition regions in the attractor. The onset and decay of blockings are also investigated to see whether collections of UPOs can be used to identify these events. In Sec. II A, we introduce the model used and then discuss in Sec. II C how we numerically found the UPOs. In Sec. III B, we describe the UPOs found in the model and how they appear to center around two clusters, and then in Sec. III C, we describe the origin of these clusters for certain parameter values. In Sec. III D, we describe how we use the UPOs to cluster the attractor, the transitions between these clusters (Sec. III E), and, finally, how we can use the UPOs to predict transitions (Sec. III F).

## II. METHODS

### A. Model

The `qgs` (quasi-geostrophic spectral) model framework[53] provides a pipeline in Python for building model equations, where a two layered quasi-geostrophic atmosphere is coupled to a choice of different bottom layers, with different degrees of interactions. The framework also allows for a flexible spectral resolution. This framework has been modified as part of this study (v1.0) and provides two key improvements over the previous version. The first is that parameters are no longer fixed with their numerical value when building the model equations,[54] allowing the parameters to be fixed when integrating the equations instead. Second, the model equations can now be returned in any desired programming language. Combined together, these two features allowed us to create a pipeline that directly feeds the model equations into continuation software to study the dynamics of the model.

In the model, the atmospheric component consists of a channel quasi-geostrophic atmosphere on a $\beta$-plane.[29,30] The model aims to simulate large scale dynamics of the midlatitudes and approximately covers the latitudes $\pm 20^\circ$ of the central latitude at $50^\circ$.

In this study, we are coupling this atmosphere to a land bottom layer, where the two components are coupled through wind stress and a thermal energy balance scheme.[55] The equations describing the evolution of the barotropic ($\psi_a$) and baroclinic ($\theta_a$) streamfunctions are

$$\begin{aligned}
&\frac{\partial}{\partial t}\left(\nabla^2\psi_a\right) + J\left(\psi_a, \nabla^2\psi_a\right) + J\left(\theta_a, \nabla^2\theta_a\right) \\
&\quad + \frac{1}{2}J\left(\psi_a - \theta_a, f_0 h/H_a\right) + \beta\frac{\partial\psi_a}{\partial x} = -\frac{k_d}{2}\nabla^2\left(\psi_a - \theta_a\right), \\
&\frac{\partial}{\partial t}\left(\nabla^2\theta_a\right) + J\left(\psi_a, \nabla^2\theta_a\right) + J\left(\theta_a, \nabla^2\psi_a\right) - \frac{1}{2}J\left(\psi_a - \theta_a, f_0 h/H_a\right) \\
&\quad + \beta\frac{\partial\theta_a}{\partial x} = -2k_d'\nabla^2\theta_a + \frac{k_d}{2}\nabla^2\left(\psi_a - \theta_a\right) + \frac{f_0}{\Delta p}\omega,
\end{aligned} \tag{1}$$

where $J$ is the Jacobian $J(f,g) = \partial_x f\,\partial_y g - \partial_y f\,\partial_x g$, $k_d$ is the friction between the ground and the atmosphere, $k_d'$ is the internal friction of the atmosphere, $h$ controls the height of the orography, and $H_a$ is the characteristic depth of the atmospheric layers. $\omega$ is the vertical velocity, which is assumed to be small in comparison with the horizontal velocity. In addition, $f_0$ is the Coriolis parameter, $\beta$ is the linear approximation from the $\beta$-plane approximation, and $\Delta p$ is the difference in pressure between the two layers.

The ground ($T_g$) and atmosphere ($T_a$) temperatures are modeled using an energy balance model,

$$\begin{aligned}
\gamma_a\left(\frac{\partial T_a}{\partial t} + J\left(\psi_a, T_a\right) - \sigma\omega\frac{p}{R}\right) &= -\lambda\left(T_a - T_g\right) + \varepsilon_a\sigma_B T_g^4 \\
&\quad - 2\varepsilon_a\sigma_B T_a^4 + R_a \\
\gamma_g\frac{\partial T_g}{\partial t} &= -\lambda\left(T_g - T_a\right) - \sigma_B T_g^4 + \varepsilon_a\sigma_B T_a^4 + R_g;
\end{aligned} \tag{2}$$

here, $\gamma_a$ and $\gamma_g$ are the heat capacities of the atmosphere and the land, $\sigma$ is the static stability of the atmosphere, $\lambda$ combines both latent and sensible heat fluxes, and $\sigma_B$ is the Stefan–Boltzmann constant. The pressure $p$ is later substituted using the ideal gas law. The solar insolation absorbed by the atmosphere ($R_a$) and ground ($R_g$) is fixed parameters. To remove the non-linear terms in the longwave radiation terms, the temperature equations are linearized ($T = T_0 + \delta T$), where $T_0$ is a fixed spatially uniform temperature and $\delta T$ is the temperature anomaly. This results in a set of equations that track the temperature anomaly.

Last, to reduce the number of model variables, a relation between the baroclinic streamfunctions and the atmospheric temperature[19] is derived from a hydrostatic relation and the ideal gas law ($\delta T_a = 2f_0\theta_a/R$, where $R$ is the ideal gas constant). We then eliminate the vertical velocity $\omega$ by combining the equations for baroclinic streamfunctions and the atmospheric temperature equations.

This collection of coupled partial differential equations is non-dimensionalized and then converted to a set of ordinary differential equations (ODEs) by projecting the model variables onto a set of basis functions, $F_i$. To force the model, we model baroclinic instability using the basis function $F_1 = \sqrt{2}\cos y$, which simulates the north–south temperature gradient, giving the solar forcing on the atmosphere as $\delta R_a(y) = C_{a,1}F_1(y)$ and similarly for the solar insolation on the ground layer. In this paper, we configure the model as described in Xavier *et al.*,[56] where we set the model resolution to be of wavenumber 2 in the $x$ and $y$ direction, resulting in ten basis functions. Here, the domain has been non-dimensionalised by dividing the coordinates by the characteristic length $L$. The model's domain is then defined over $(0 \le x \le 2\pi,\ 0 \le y \le \pi)$, where $n$ is the aspect ratio between the meridional and zonal extents, defined by $n = 2L_y/L_x$. The land and atmosphere use the same basis. The key parameter values used are given in Table I. The resulting final model equations, and the basis modes used in this study, are presented in Sec. S-I.A of the supplementary material.

Zonal flow corresponds to times when the flow is directed from west to east. The atmosphere is considered blocked where a high amplitude ridge exists either to windward or leeward of the idealized orography, which is analogous to blocking patterns seen in

**TABLE I.** Unless otherwise stated, the model is set with the above parameter values.

| Parameter | Value | Description |
|---|---|---|
| $\varepsilon_a$ | 0.76 (nondimensional) | Atmospheric emissivity |
| $k_d$ | 0.085 (nondimensional) | Friction between the atmosphere and the ground |
| $k_d'$ | 0.02 (nondimensional) | Internal friction between the two layers of the atmosphere |
| $C_{g,1}$ | $300\,\mathrm{Wm^{-2}}$ | North–south gradient of solar forcing on ground |
| $C_{a,1}$ | $\frac{4}{10}C_{g,1}\,\mathrm{Wm^{-2}}$ | North–south gradient of solar forcing on atmosphere |
| $\gamma_a$ | $1\times10^7\,\mathrm{Jm^{-2}K^{-1}}$ | Heat capacity of atmosphere |
| $\gamma_g$ | $1.6\times10^7\,\mathrm{Jm^{-2}K^{-1}}$ | Heat capacity of ground |
| $\lambda$ | $10\,\mathrm{Wm^{-2}K^{-1}}$ | Sensible and turbulent heat transfer |
| $\sigma_B$ | $5.67\times10^{-8}\,\mathrm{Jm^{-2}\,s^{-1}\,K^{-4}}$ | Stefan–Boltzmann constant |
| $\sigma$ | 0.2 (nondimensional) | Static stability of the atmosphere |
| $n$ | 1.3 (nondimensional) | Aspect ratio ($n=2\,L_y/L_x$) |
| $f_0$ | $1.032\times10^4\,\mathrm{s^{-1}}$ | Coriolis parameter |
| $\beta$ | $1.3594\times10^{-11}\,\mathrm{m^{-1}s^{-1}}$ | $2\Omega\cos(\phi_0)/a$ ($\phi_0$: reference latitude, $a$: radius of the Earth) |
| $\Delta p$ | 500 hPa | Difference in pressure between the two layers |

the North Pacific.[57] Here, the orography is modeled as a mountain and valley, using the $F_2 = 2\cos(nx)\sin(y)$ mode, where the resulting orography profile is shown in Fig. 9. As in Charney and DeVore,[28] specific barotropic streamfunction modes can provide a description to determine the atmospheric state of the atmosphere. Blocking in the atmosphere, or the presence of a large amplitude wave, points toward an east–west orientated double gyre in the barotropic streamfunctions. Given the highly truncated nature of this model, this points toward high amplitudes of the barotropic modes $\psi_{a,2}$ and/or $\psi_{a,3}$, which correspond to modes $F_2$ and $F_3 = 2\sin(nx)\sin(y)$. On the other hand, zonal flow is expected to have low magnitudes over these modes.

Further information on the bifurcation structure of the fixed points and sensitivity to model properties can be found in Li *et al.*[55] For further information on predictability of the different regimes for altering parameter values, see Xavier *et al.*[56]

## B. Lyapunov analysis

To analyze the stability properties of the chaotic attractor, we have calculated the Lyapunov exponents of the system. In this study, we calculate the backward Lyapunov exponents, using *QR* factorization of the tangent linear propagator,[58] or orthogonalization. This involves integrating the system and the tangent linear model forward in time and factorizing the matrix basis of perturbations of the linear model. At each time step of the integration, we can calculate the instantaneous (also called local or finite-time over one time step) Lyapunov exponents by taking the natural logarithm of the expanding and contracting directions and dividing by the length of the time step, $\tilde{\lambda}_i = \ln(r_{ii})/(t_{n+1} - t_n)$, where $r_{ii}$ is the $i$th diagonal entry of the matrix $R$, which is obtained from the *QR* factorization. The Lyapunov exponents are of decreasing magnitude. Each column of the matrix $Q$ provides the instantaneous Lyapunov vector. As time goes to infinity, the average of $\tilde{\lambda}_i$ will approach the $i$th backward Lyapunov exponent.[59]

The instantaneous Lyapunov horizon can be used to understand the regions of the state space that display greater levels of predictability, compared with the remainder of the chaotic attractor. The instantaneous Lyapunov horizon is calculated by taking the inverse of the instantaneous Lyapunov exponent and is, therefore, measured in units of time. The Kaplan–Yorke dimension[60] measures the dimension of the chaotic attractor. Here, we define an instantaneous (or local) Kaplan–Yorke dimension as $D = j + \sum_{i=1}^{j}\tilde{\lambda}_i/|\tilde{\lambda}_{j+1}|$ where $j$ is the largest index such that $\sum_{i=1}^{j}\tilde{\lambda}_i > 0$. The dimension of the attractor provides information about the number of expanding dimensions and, thus, provides a way of quantitatively characterizing the stretching and contracting regions of state space.[61]

## C. Numerically finding UPOs

In this paper, we have used two methods for finding UPOs: the Newton–Raphson method and the continuation software AUTO.[62] The Newton–Raphson method[63,64] aims to solve the equation $S^t(\mathbf{x}_0) = \mathbf{x}_0$, where the unknowns are the starting location in state space ($\mathbf{x}_0$) and the time $t$. This method has been described in numerous studies to numerically calculate UPOs.[46,65–68] Following Gritsun,[51] we have used the second order tensor method, which aids in finding UPOs in this system where there are a large number of close to zero Lyapunov exponents.[69] In this case, due to unstable dimension variability[70] or a breakdown in hyperbolicity, the region of convergence can be very small, and the second order method, though approximately ten times more computationally expensive, can aid with finding UPOs[71] in these circumstances. The algorithm used, and convergence criteria, is described in Sec. S-II of the supplementary material.

We also used the software AUTO to find UPOs via continuation across parameters. This software was chosen for its extensive track record for bifurcation analysis in relatively high dimensional systems, but several other suitable continuation software options are available (for example, Veltz[72] and Clewley *et al.*[73]). This was done by first numerically finding the fixed points of the model. We tracked these fixed points for several key parameter values. At any Hopf bifurcation points, we then branched and followed the periodic orbit branches. We continued to follow branches at branching

points or period doubling from these periodic branches. This process was done for up to 50 branches deep. This process was aided by the auto-AUTO Python package.[74] This package acts as a layer on top of AUTO and automates the branching and identifies which branches to follow.

### D. Initial conditions

The Newton–Raphson method can be very sensitive to initial conditions. This means that which UPO you end up on, or whether you end up on a UPO at all, is highly dependent on the initial conditions fed into the algorithm. The initial conditions refer to the starting location of the closed loop in state space and the initial guess at the period of the closed loop. If the state space is of dimension $n$, the initial condition is of dimension $n + 1$. In this study, we used the following four methods to guess initial conditions:

#### 1. Random initial conditions

The initial conditions, the starting location in space and the period, were chosen randomly. We used a uniform distribution, where the bounds of the uniform distribution were set by finding the bounds of the attractor. Here, we set the maximum period to be 225 days. This upper bound on the period was set as the probability of finding longer period UPOs is low.

#### 2. Near misses

We first ran a very long trajectory. We then passed a sliding window of length 225 days over this trajectory, and by calculating a norm between every point within this sliding window, we determined points ($\mathbf{x}_0$) where after some time $t_i$, the trajectory passes sufficiently close to itself again: $\left\| S^{t_i}(\mathbf{x}_0) - \mathbf{x}_0 \right\| < \varepsilon$. This provided us with a guess of the period ($T_0 = t_i$) and the starting point in space $\mathbf{x}_0$.

#### 3. Perturbed UPOs

Starting from a UPO, we take a random point on the UPO and perturb the point and the period. We use this perturbed point as a new initial condition and feed this to the algorithm. This utilizes the fact that UPOs should be dense in the attractor, so there should be another UPO living close to the given one. Usually, this will result in the method producing the original UPO, so a filter needs to be used to ignore the result if it does not produce a new UPO.

#### 4. UPO continuation

UPOs could be found for certain parameter values more easily than others, in certain regions of the state space. This can occur when there is a change in the stability landscape of the attractor for different parameter values, specifically when the attractor is not hyperbolic or when there are UPOs present with different numbers of stable dimensions or unstable dimensional variability.[75–77]

This method takes advantage of this by first finding a UPO at parameter values where it is easier to do so. Continuation software is then used to track the UPO back to the sought after parameter values. In our case, we used the work of Xavier *et al.*[56] to understand for which parameter values the largest Lyapunov exponent was close to zero, suggesting that the flow is diverging more slowly at these values. We then used the Newton–Raphson method to find UPOs for these parameter values and tracked these branches back to the original values using AUTO. This method will fail when the branch does not extend to the desired parameters either due to a fold bifurcation or the continuation software not being able to track the branch.

## III. RESULTS

### A. Model behavior

The model climate displays both zonal as well as blocked weather regimes. These differing weather regimes occur quasiperiodically, as the trajectory travels around the single attractor. The blocked regimes consist of two distinct behaviors: one where the blocking occurs to windward of the orography and the other to leeward. The model is chaotic and has three positive Lyapunov exponents [Fig. 1(a)] but is dissipative with large negative exponents. There exists a plateau of close to zero Lyapunov exponents, likely resulting from the longer timescales in the ground heat capacity, compared with the atmosphere.[56] This plateau results in regions of the attractor that display significant differences in an instantaneous Kaplan–Yorke dimension. This, along with information about the instantaneous Lyapunov exponents, shows that regions of the chaotic attractor display differing rates of convergence and divergence and, as a result, persistence.

There are particular projections of the 30 dimensional state space that make intuitive sense for studying atmospheric blocking regimes. As discussed in Sec. II A, we are interested in the magnitudes of the barotropic streamfunctions ($\psi_{a,2}$, $\psi_{a,3}$). By analyzing the climatology of the model, we found that there is a temperature anomaly in the ground, which displays low frequency variability, moving from east to west with quasiperiodic behavior. This anomaly results in, on average, a greater level of blocking in the region of the atmosphere above the temperature anomaly. This can be tracked by observing the magnitude of the variable $\delta T_{g,3}$. When the temperature anomaly transitions from one side of the domain to another, the atmosphere can display zonal atmospheric behavior, or transitions between leeward and windward blocking regimes. A projection on the variables ($\psi_{a,2}, \psi_{a,1}$) has been used before for studying similar baroclinic two layer atmospheres.[30] This projection identifies a particular large magnitude barotropic streamfunction that corresponds to blocking systems. However, this projection does not cleanly present the low frequency variability in the ground temperature. When the chaotic attractor is projected onto the variables ($\delta T_{g,3}, \psi_{a,2}$), shown in Fig. 2(a), two main clusters are visually present. The clusters seen on the left and right designate regions where averaged behavior displays, on average, atmospheric blocking behavior, driven by the orography and the temperature in the ground. Last, we also analyzed the results using the projection ($\delta T_{g,3}, \psi_{a,1}$), and while we found the same two distinct clusters, the transitions between these clusters could not be as cleanly disentangled. We present the different combinations of the projections in Fig. S2 of the supplementary material. We present the blocking in the model atmosphere in Fig. 9 and the ground temperature anomalies in Fig. S1 of the supplementary material.

### B. Key unstable periodic orbits

We found 6818 UPOs in total, using the methods described in Sec. II C. These UPOs are primarily centered on top of the two dense

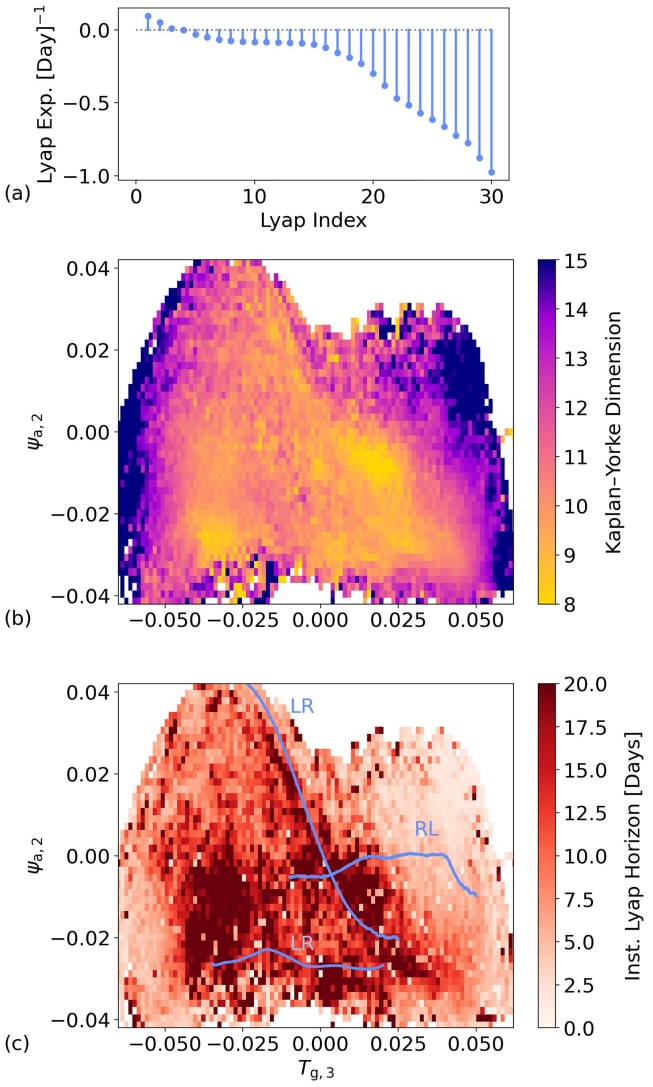


**FIG. 1.** Lyapunov analysis of the chaotic attractor. Subplot (a): The Lyapunov spectra. Subplot (b): Instantaneous Kaplan–Yorke dimension. Subplot (c): Binned instantaneous Lyapunov horizon, or the inverse of the binned instantaneous Lyapunov exponents, averaged over each pixel. The averaged transition trajectories (see Sec. III E) are shown, with two transitions from the left to right cluster (LR) and one from right to left (RL).

clusters, designating a high temperature anomaly in the ground, which results in one of the two key weather regimes described above. The Newton method primarily found UPOs in regions where model trajectories remain for extended time periods. This is likely due to adequate initial conditions being more probably to encounter. We could not find any UPOs that link the two central clusters. This is likely because such orbits would either have periods longer than the maximum searched for (set to 225 days as beyond this, the algorithm converged extremely slowly), or either because no such orbits exist or they exist in a narrow band in space and period length making it difficult to find numerically.

In Fig. 2(b), we show the projection of the UPOs that we found on the attractor. This shows how the UPOs appear to form dense sets over the dense areas in the attractor. It is expected that such numerical searches for UPOs will be biased toward short period UPOs, as long as period UPOs are numerically more difficult to find.[32] In our case, however, we have found a similar number of UPOs between periods of 4–100 days, as shown in Fig. 2(c). In addition, we see a large range in the largest Floquet exponent [Fig. 2(d)], meaning that there is a large range in the stability properties of the clusters. This is clearly not a complete set of UPOs for these periods, and the skew in the period of the resulting UPOs found is likely due to the most common repeating cycles in the key variables ($\delta T_{g,3}$, $\psi_{a,2}$). This is not unexpected, as the numerical method we employ is highly sensitive to the initial conditions used. In our case, the initial conditions were primarily found by looking for close recurrences in the trajectory, which, in turn, is driven by natural cycles in these variables.

## C. Origin of blocking clusters

To understand why our model contains these two regimes, we undertook bifurcation analysis of the model for varying $k_d$ and $C_{g,1}$, as varying these parameters resulted in the finding of stable periodic solutions in the center of these clusters, in the work by Xavier *et al.*[56] We have developed on this previous work by using AUTO[62] to investigate the bifurcation structure that originates from these two stable windows. Figure 3 shows the bifurcation diagram as a function of $k_d$. The same analysis for altering $C_{g,1}$ is presented in Sec. III of the supplementary material. These bifurcation diagrams were produced by numerically finding fixed points of the model and continuing along all branches, and following any subsequent branching points. We branched at any detected Hopf bifurcation points, again continuing along branches originating from periodic orbit branching points or period doubling bifurcations. This process was automated using the auto-AUTO package. Last, we also continued the periodic orbit branches, from the UPOs found numerically using the Newton–Raphson method, described in Sec. II C, and included these in the bifurcation diagram.

There exists a window, at approximately $k_d \approx 0.1045$ and $k_d \approx 0.115$, where periodic orbits living in the LHS cluster become stable. We used AUTO to track these orbits to investigate how they destabilize and whether they can give a hint at how chaos emerges. In Fig. 3, we show these regions of stability on the bifurcation diagram. The continuation parameter is plotted against the maximum $L^2$-norm. The $L^2$-norm $\left(|x_i| = \sqrt{\sum_j \left[\overline{S_i^T}\right]_j^2}\right.$, where $j$ is an index over the dimension and $i$ is an index over the collection of UPOs$\left.\right)$ was chosen to retain continuity with previous studies.[19] We see that there is a closed branch (shown in light blue), which goes through a period doubling bifurcation, and leads to another branch (shown in dark blue) that has a small window of stability before destabilizing through a torus bifurcation. The bifurcation diagram shows that this structure has a similar value in $L^2$ norm space to the other periodic orbit branches. This means that while we cannot see how these key branches connect to the rest of the bifurcation diagram,

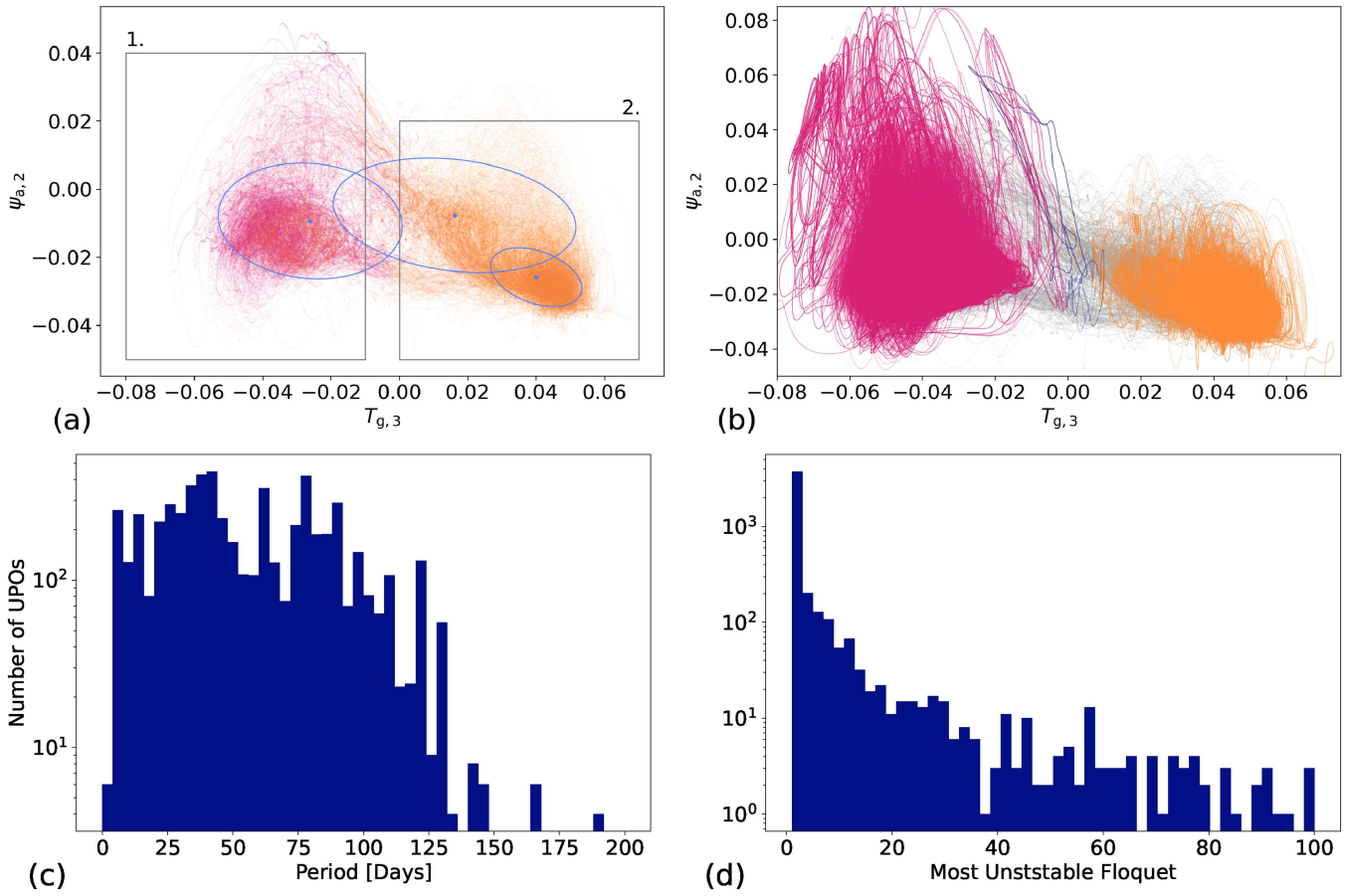


**FIG. 2.** Key UPO properties for all UPOs found. Subplot (a) shows the chaotic attractor of the model, with points showing the time steps of a trajectory, where the two colors (pink and orange) show the clustering of the attractor using the distance from UPOs. The Gaussian mixture clustering clusters are shown in blue, calculated as described in Xavier *et al.*[56] We present the climatology of the three centroids in Fig. S1 of the supplementary material. The gray inset boxes display the extents of (1): Fig. 4 and (2): is shown in Fig. S4 of the supplementary material. Subplot (b) shows the UPOs projected on top of the attractor, again colored based on the clusters. Subplots (c) and (d) show compiled information on the periods and largest Floquet exponents of the identified UPOs. The number of unstable dimensions of the collection of UPOs range between 1 and 6, pointing to violations of hyperbolicity.[47] Subplot (a) was modified from Xavier *et al.*, Earth Syst. Dyn. **15**(4), 893–912 (2024). Copyright 2024 Author(s), licensed under a Creative Commons Attribution (CC BY) License.[56]

we hypothesize that these branches originate from a torus bifurcation of another branch, a guess that is reinforced by the visual similarity between these orbits and other orbits that we found in this cluster.

In Fig. 4 we show key UPOs, from the left hand cluster, for decreasing values of $k_d$. Two particular UPOs are colored to match the coloring in the bifurcation diagram shown in Fig. 3, all other periodic orbits are shown in gray. The blue UPOs appear to occupy the central section of the cluster defined by the UPOs, and we see that this structure remains even once the colored periodic orbit branches go through a fold bifurcation and disappear for lower values of $k_d$. Similar analysis for the right hand side cluster is provided in Sec. S-III of the supplementary material, with the bifurcation diagram for $C_{a,1}$ shown in Fig. S3 of the supplementary material and the change in UPOs as a result of altering the value of this parameter shown in Fig. S4 of the supplementary material. This analysis shows that key branches provide a hint at the origin of the cluster dynamics that we find in this model.

### D. Clustering the attractor

In this study, we use the UPOs to assign each point of a trajectory into the left and right hand clusters identified and shown in Fig. 2(a). We are interested in doing this, as it provides a classification of whether we are in a windward or leeward blocking regime, and allows us to identify the onset and decay, or transitions, between these regimes. This is done by first splitting the UPOs into two clusters dependent on if they have positive or negative values of $\delta T_{g,3}$. More precisely, we analyze the maximum and minimum values of each UPO on the variable $\delta T_{g,3}$, which is the ground heat projected

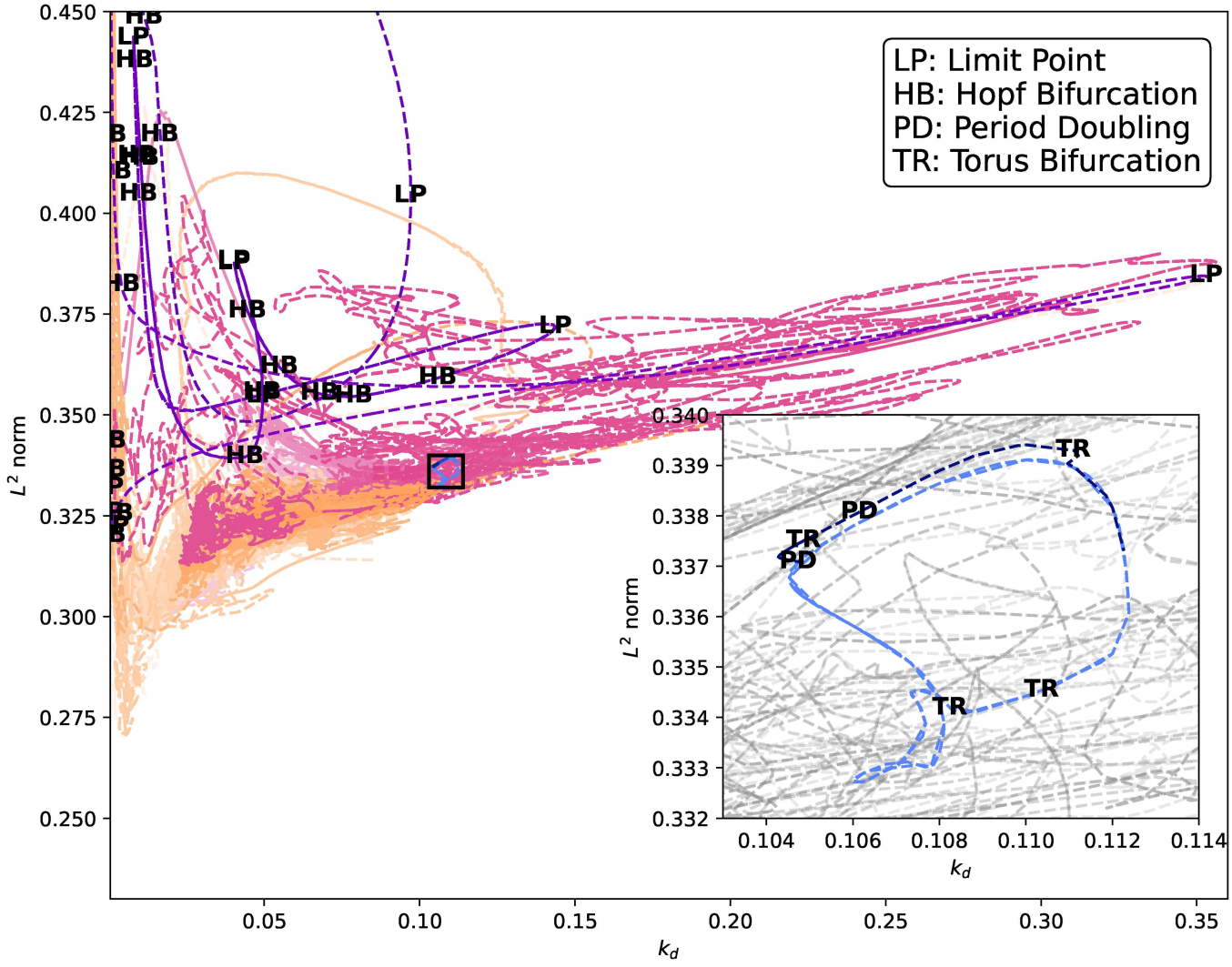


**FIG. 3.** Bifurcation diagram of all fixed points (shown in purple) and the branching periodic orbits (shown in orange and pink to visualize the two separate clusters) of the model for varying $k_d$ with a value of $C_{a,1} = 300\ \mathrm{Wm}^{-2}$. Dotted lines represent unstable regions, and solid lines represent stable regions. Bifurcation points are shown for the fixed point continuations. The black rectangle is zoomed in and shown in the inset and focuses on two key branches shown in blue. These two periodic branches were found by continuing periodic orbits that have a small window of stability. The light blue branch is stable at $k_d \approx 0.112$ and the dark blue at $k_d \approx 0.1045$.

onto the mode $F_3 = 2\sin(nx)\sin(y)$,

$$\text{LHS Cluster UPOs}: \ C^{\text{UPO}}_{\text{LHS}} = \left\{ \overline{S^T_i} : \max_{\delta T_{g,3}} \overline{S^T_i} < 0,\ i \in I \right\},$$

$$\text{RHS Cluster UPOs}: \ C^{\text{UPO}}_{\text{RHS}} = \left\{ \overline{S^T_i} : \min_{\delta T_{g,3}} \overline{S^T_i} > 0,\ i \in I \right\},$$

where $\overline{S^T_i}$ is a UPO with a period $T$ and an index $i$, and $I$ is an indexing of all UPOs found. This results in 3425 UPOs in the left hand cluster and 3361 on the right (32 UPOs do not fall into either cluster and are ignored). Next, for a given trajectory $S^t(\mathbf{x}_j)$ with initial condition $\mathbf{x}_j$, we cluster the points of the trajectory $(S^{t_k}(\mathbf{x}_j))$ by calculating which cluster the UPO, that is closest to the trajectory point, is a member of

$$\text{LHS Cluster Trajectory}: \ C^{S^t}_{\text{LHS}} = \left\{ S^{t_k}(\mathbf{x}_j) : \min_{i \in I} \left\| S^{t_k}(\mathbf{x}_j) - \overline{S^T_i} \right\|, \ \overline{S^T_i} \in C^{\text{UPO}}_{\text{LHS}} \right\},$$

$$\text{RHS Cluster Trajectory}: \ C^{S^t}_{\text{RHS}} = \left\{ S^{t_k}(\mathbf{x}_j) : \min_{i \in I} \left\| S^{t_k}(\mathbf{x}_j) - \overline{S^T_i} \right\|, \ \overline{S^T_i} \in C^{\text{UPO}}_{\text{RHS}} \right\},$$

where the notation $\|\cdot\|$ stands for the Euclidean norm.

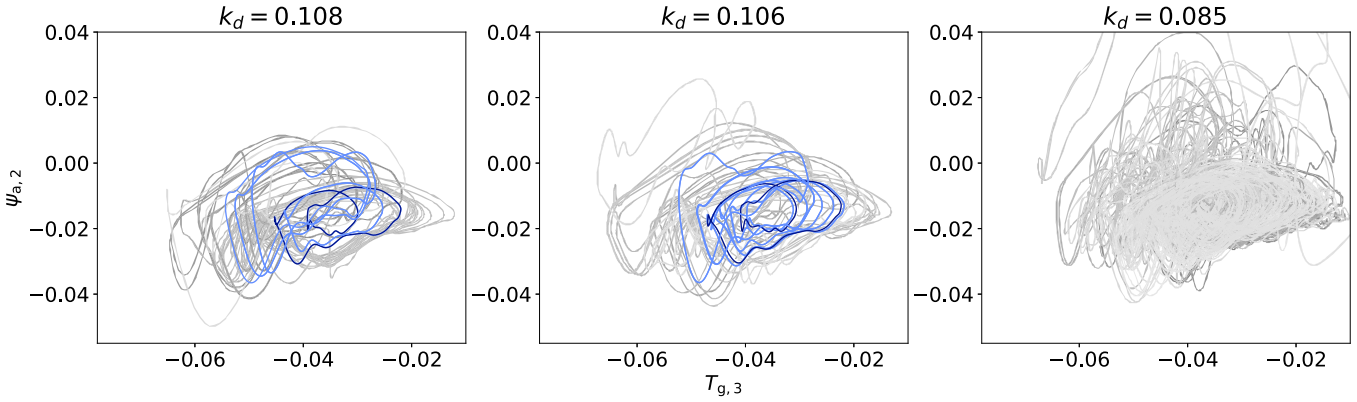


**FIG. 4.** State space for variables ($\delta T_{g,3}$, $\psi_{a,2}$) for decreasing values of $k_d$. The orbits shown in blue correspond to the branches shown in the inset plots of Fig. 3. Gray orbits show that the other branches found that do not directly branch from the key orbits. On the left, we show the parameter values where a stable orbit was found, and we then decrease the parameter values to end up with the clusters, as shown in Fig. 2(b). Extents, relative to the entire attractor, are shown in Fig. 2(a).

The clustering is visualized by the color scheme (pink and orange) in Fig. 2(b). As we see, this is not as simple as just clustering the points of the trajectory by the value of $\delta T_{g,3}$ as in other projections, the UPOs are not neatly separated. We think that this clustering method is optimal as the UPOs form a dense skeleton in the dense region of the attractor, and by clustering on which UPO a trajectory point is closest to, it is expected that the UPO should provide some description as to the flow in that neighborhood. Of course, this approach is dependent on the number of UPOs found and how close the trajectory is to a given UPO. If few UPOs are found, the attractor is not described in any real detail, and if the trajectory is far from a UPO, then there is no reason to believe that the closest UPO will have any influence on the trajectory.

We expect that our approach is robust to the above concerns. It has been found in that a surprising low number of UPOs still provides reasonable results.[44] In our case, there are clearly multiple distinct regimes within the single attractor,[56] and the clusters found here overlap well with those found in this earlier study. We believe that our clustering method provides a cleaner method for isolating transitions as it is not a probabilistic clustering method and provides information influenced by the system dynamics. In addition, it provides a measure between a point of the trajectory and the cluster of UPOs that covers the dense regions of the attractor. This distance, therefore, provides a useful metric for identifying transitions, as well as providing information on how much we expect the cluster of UPOs to affect the behavior of a trajectory.

On average, trajectories in the pink regime of the attractor correspond to a windward blocking pattern in the atmosphere, which can be visualized in the first panel of Fig. 9(a) and the last panel of Fig. 9(c). The orange regime corresponds to leeward blockings, which can be seen in the last panel of Fig. 9(a) and the first panel of Fig. 9(c).

### E. Transition paths

Transitions between the two regimes of the attractor occur through specific regions, or channels, of the state space, shown in Figs. 5(a) and 5(b). These transitions correspond to a shift in the ground temperature anomaly and, thus, whether the climate displays windward or leeward blocking behavior. The transitions are identified by the points in the state space where a trajectory passes from one cluster to another and by analyzing the points on the trajectory that precede and follow the transition. To analyze the properties of these transitions, we began by running a long trajectory and then isolating the occurrences where a transition occurs. To ensure that we are capturing transitions between the regimes, we filter the points to ensure that a trajectory remained in one cluster for at least 56 days before and 56 days in the other cluster after transitioning. This threshold is set to remove points that are in between the two sets of UPOs and are, therefore, not described well by our clustering method (approximately 0.07% of points).

By parameterizing on $\delta T_{g,3}$, we created averaged transition trajectories to analyze the climatology of these paths. Transitions from the LHS (left hand side) to RHS cluster appear to pass through two regions, and the averaged trajectories shown are the transitions between two blocking regimes. This is primarily driven by the ground temperature anomaly shifting between the east and west. The transition in the lower portion of the attractor, shown in Fig. 6(a), displays the blocking regime moving to the west, which can be seen in the model climatology shown in Fig. 9(a). The other left to right transition taking place in the upper part of the attractor [Fig. 7(a)] shows the blocking regime moving to the east [Fig. 9(b)].

Transitions from the RHS to LHS are not as clearly defined in state space [shown in Fig. 5(b)], but the averaged transition [Fig. 8(a)] shows that the transitions between the two blocking regimes result in averaged zonal behavior in the atmosphere. This is not surprising as the transition paths pass close to the Hadley circulation or the origin. In Xavier *et al.*,[56] the zonal regime was identified as a separate cluster, but in our analysis, we find that this atmospheric regime primarily occurs during transitions between the RHS cluster and the LHS cluster, as shown in Fig. 9(c). The difference between transition types has been observed before by Grafke and Vanden-Eijnden,[78] who used an action minimization

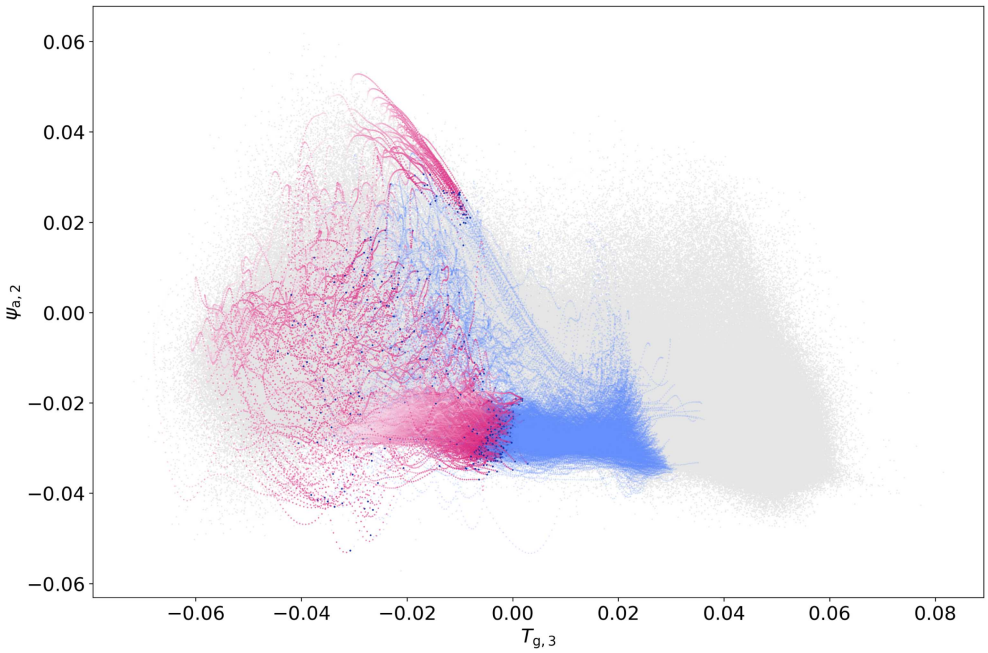


(a)

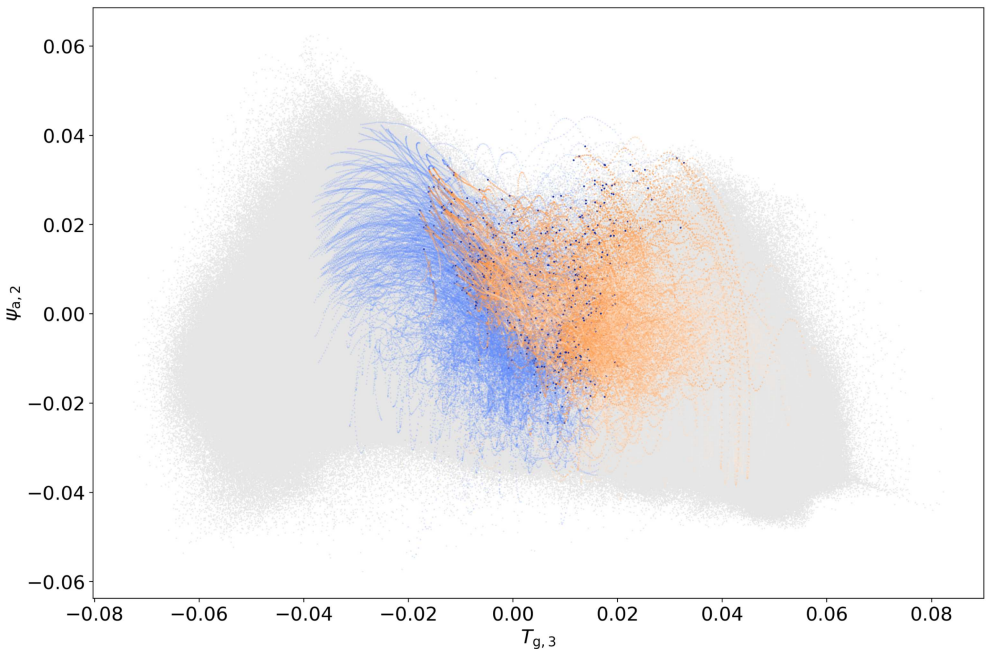


(b)

**FIG. 5.** Transitions from one cluster to the other: Fig. 5(a) shows transitions from left to right and Fig. 5(b) from right to left. The trajectory is shown 11 days before the transition (in pink or orange, where the saturation increases toward the transition). The transition points are shown in navy blue, and the post-transition trajectory is shown in light blue for 11 days after the transition.

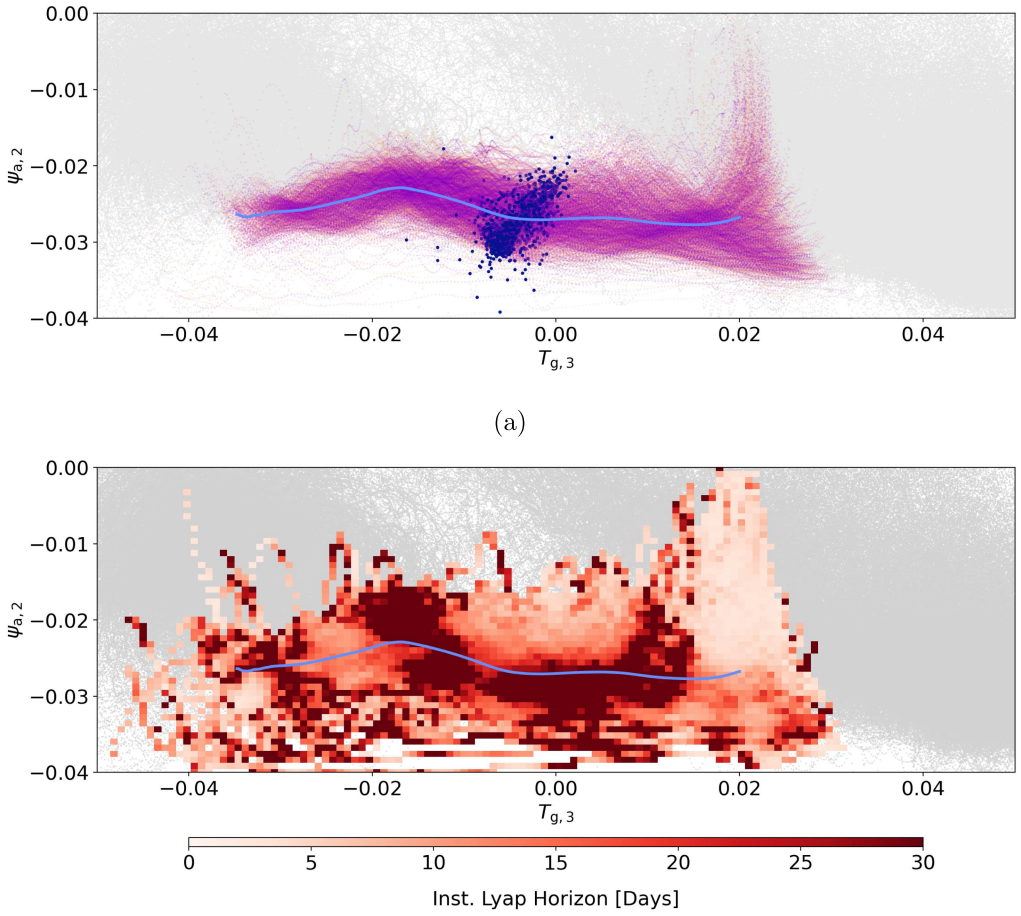


**FIG. 6.** Left to right transitions, taking place in the lower section of the attractor. Figure 6(a) shows the filtered trajectories that transition from left to right in the lower portion of the attractor. The mean of these trajectories is shown in light blue. The transition points are shown in navy blue. Figure 6(b) displays the binned instantaneous Lyapunov horizon, calculated by taking the inverse of the binned instantaneous Lyapunov exponent.

algorithm to find the most likely noise induced transition paths between blocked and zonal states in the barotropic model of Charney and DeVore.[28] They found that transitions from blocked to zonal and zonal to blocked regimes are not merely the time-reversed forward transition, implying that time-reversal symmetry is broken and highlighting the nonequilibrium nature of the transition.

Finally, 55% of transitions between regimes do not occur through the regions described above. These transitions occur for trajectories that spend short time in a given regime (less than 56 days). These transitions do not appear to follow predictable behavior and are probably due to the trajectory making diversions in other dimensions, and the transitions only appear to occur due to the projection we make onto two dimensions.

The paths of the transitions were found to occur through relatively stable regions of the state space. This is shown in Figs. 6(b), 7(b), and 8(b), which show the Lyapunov horizon, calculated by taking the instantaneous Lyapunov exponent for each transition, binning the results in state space, and then taking the inverse of the results. This shows that while the onset of the transition occurs through an unstable region, once the trajectory begins transitioning from one regime to another, the path it takes, and therefore, the atmospheric behavior is more predictable.

The transition paths identified in this study have qualitative similarities with transition channels seen in other systems with self-induced switching behaviors. Ansmann *et al.*[79] found that, in a network of diffusively coupled FitzHugh–Nagumo oscillators, switching between different dynamics was facilitated by channel-like structures on a chaotic saddle,[80] and the opening of the channel can be studied by computing the stable and unstable manifolds of the fixed point associated with the mechanism of the emergence.[81,82] In the context of climate models, similar channels have been found in paths of extreme events in an ENSO model.[83]

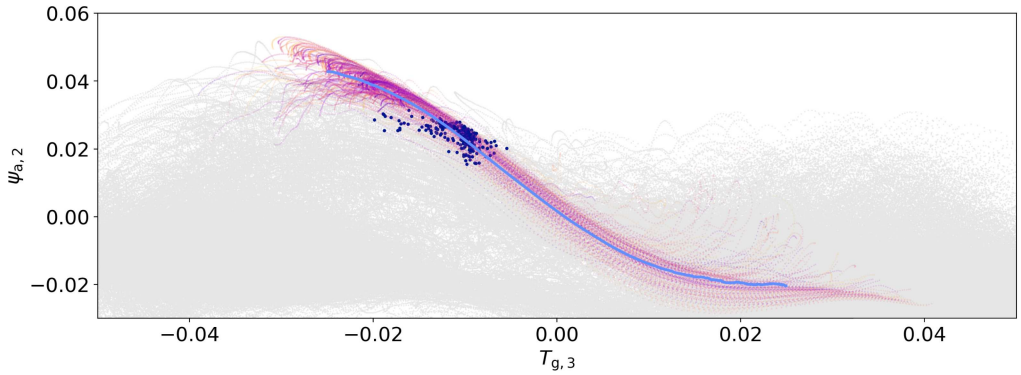


(a)

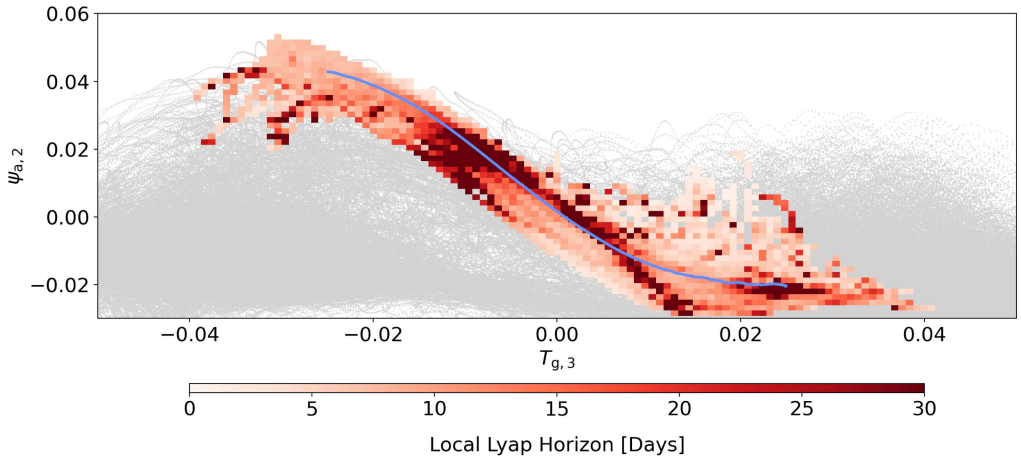


(b)

**FIG. 7.** Upper left to right transition. Figure 7(a) shows the filtered trajectories that transition from left to right in the upper section of the attractor, shown in Fig. 5(a), with the same color scheme. Figure 7(b) shows the same as Fig. 6(b), but again for the upper left to right transition.

### F. UPO shadowing

The trajectory moves between the two clusters, sometimes spending a long time in one regime (up to 1000 days in the RHS cluster and 600 days in the LHS), other times quickly returning back to the previous regime. Above, we showed that when a trajectory spends long times in one regime and then transitions to the other regime, it tends to pass through a well-defined region in the state space. We now look at which collection of UPOs the trajectory passes close to during its visit to a cluster. The idea being that if the transition path appears to be confined in state space, the trajectory must pass close to a specific set of UPOs while transitioning. As UPOs are dense in the attractor, the UPOs can provide an arbitrarily accurate approximation for a given trajectory.[46] The idea of looking at UPOs close to the trajectory, to gain some understanding of the future path the trajectory will take, is referred to as UPO shadowing. In our case, we have only found a small selection of UPOs so the accuracy of any shadowing will be limited, but the idea remains the same; a UPO will shadow a trajectory if they are close to one another, and for some limited time, the evolution of the trajectory is similar to that of the UPO.

More concretely, a UPO $\overline{S_i^T}$ shadows the trajectory at time $t$ if it is the closest UPO, of all UPOs found, to the location of the trajectory at time $t$: $\min_{i\in I} \left\| \overline{S_i^T} - S^t(\mathbf{x}_j) \right\|$, where $I$ is an index of all the UPOs. Here, we are assuming that we can create an index of the UPOs as numerically we can only find a finite number of UPOs, the method of indexing the UPOs is arbitrary. We are interested in which UPO is the closest at a given time, so we define a function $\mathrm{ind}(S^t(\mathbf{x}_j))$, which returns the index of the UPO, given the trajectory point $S^t(\mathbf{x}_j)$, where $\mathrm{ind} : \mathbb{R}^n \to I$, and $I$ is the indexing set of the UPOs.

We define the number of times that a given UPO shadows a trajectory over a set period of time, which we call cumulative

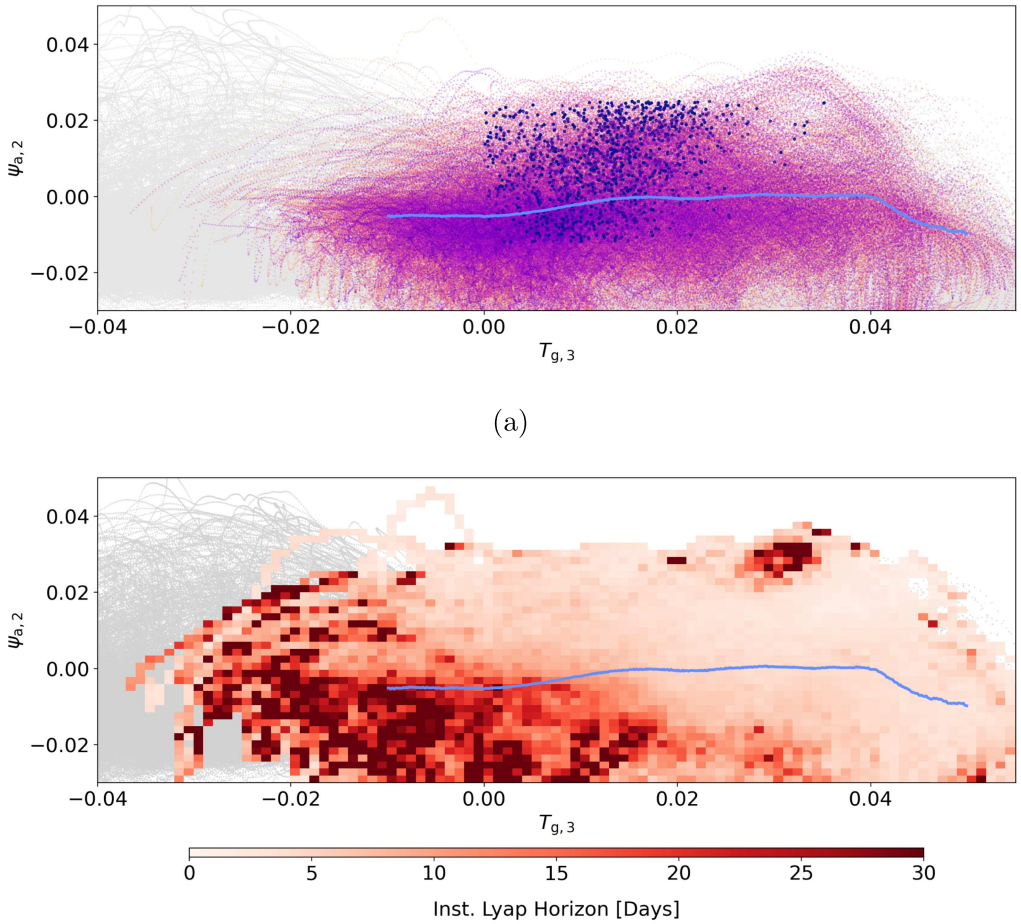


**FIG. 8.** Right to left transition. Figure 8(a) shows filtered transition trajectories. The mean of these trajectories is shown in light blue. The transition points are shown in navy blue. Figure 8(b) displays the same as Fig. 6(b), but for the right to left transition.

shadowing (CS). This is done by counting the number of times a given UPO $\overline{S_i^T}$ shadowed the trajectory in the time range $(t_1,\ t_2)$, expressed as

$$\Omega\left(\overline{S_i^T},\ t_1,\ t_2\right) = \sum_{t\in[t_1,t_2]} \delta\Big(i,\ \mathrm{ind}\left(S^t(\mathbf{x}_0)\right)\Big), \tag{3}$$

where $\delta$ is the Kronecker delta, and returns 1 if the closest UPO has index $i$, otherwise returns 0.

Looking at trajectories that spend long time periods (at least 110 days) in only one cluster, we found at least three distinct sets of UPOs: one where the CS increases primarily when the trajectory first enters the cluster (called Pre-Blocking), another set where the CS mainly increases before a transition (called Transition), and a final set where the CS mainly increases in between entering and transitioning from the regime (called Blocking). We show these three distinct sets of UPOs for the LHS cluster in Fig. 10. In this figure, we also show the CS for each set of UPOs, during the time period just after a transition and just before a transition. We see that there is a step change in the slope of the CS for the different sets, depending on the proximity to a transition. We present similar analysis for the RHS in Fig. S5 of the supplementary material. We set a minimum time for the trajectory to spend in one cluster because, as we showed in Sec. III E, trajectories that do not spend enough time in either cluster tend to not transition through the specified regions, meaning that one cannot predict these transitions with only three groups of UPOs.

In Fig. 11, we show three example time series of the trajectory and the CS for each one. We see in these examples that before the transition, there is a clear increase in the CS of the Transition set of UPOs, while the CS of the Blocking set plateaus. In addition, we show the CS of the Pre-Blocking set shows that the largest increase before the trajectory settles onto the set of Blocking UPOs. This method is dependent on the trajectories traveling along the

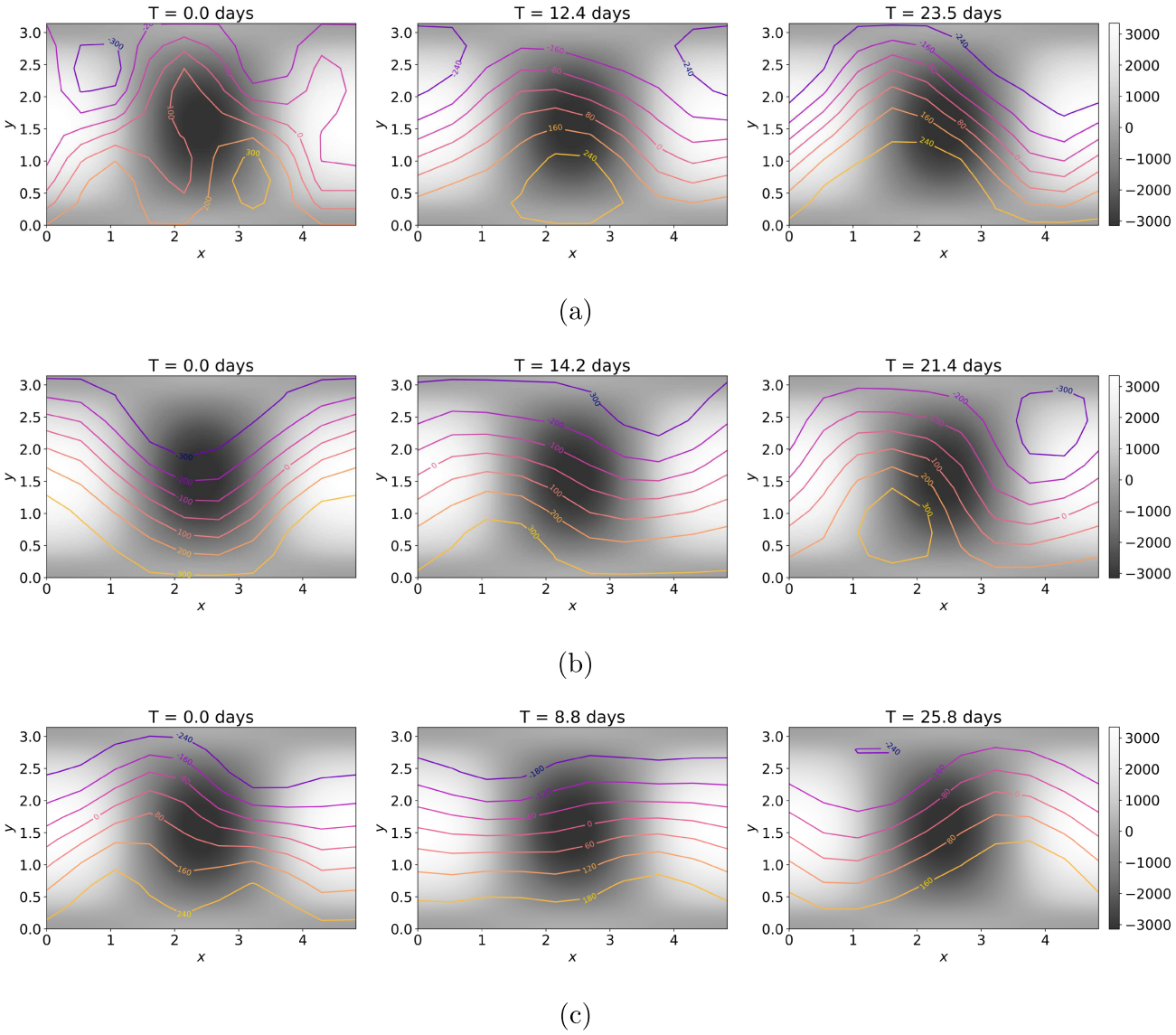


**FIG. 9.** Snapshots of the climatology of the averaged transition trajectories. The model time of each snapshot is shown in the title. The contours show the 500 hPa height anomaly, and the grayscale shading shows the relative height of the orography in meters. The 500 hPa height anomaly is commonly used to determine regions of blocking, as higher anomalies correspond to high pressure systems.[8] (a) Transition from left to right in the lower portion of the attractor, shown in Fig. 6(a). Here, the average blocking behavior transitions from the windward side of the orography to the leeward side by traveling to the west. (b) Transition from left to right in the upper portion of the attractor, shown in Fig. 7. The blocking transitions from above the orography to the leeward side by traveling to the east. (c) Transition from right to left, as in Fig. 8(a). Here, the blocking moves from the leeward side of the orography to the windward side through zonal atmospheric behavior.

described channels in state space. Transitions of trajectories that do not remain in one cluster for long periods of time transition through other, less predictable, regions, and this method cannot be used to provide a warning signal. In addition, depending on where the trajectory exits the cluster of UPOs, the early warning indicator provides more or less warning of the impending transition. An example of this can be seen in Fig. 11, where the Transition set increases at a different number of days before the transition occurs, thus not providing a regular warning. Last, the accuracy of this method is dependent on the number of UPOs used, and it is possible that we are missing some orbits that would further improve the accuracy. Overall, the proposed method of using CS could provide a useful early warning indicator for transitions between clusters of the attractor.

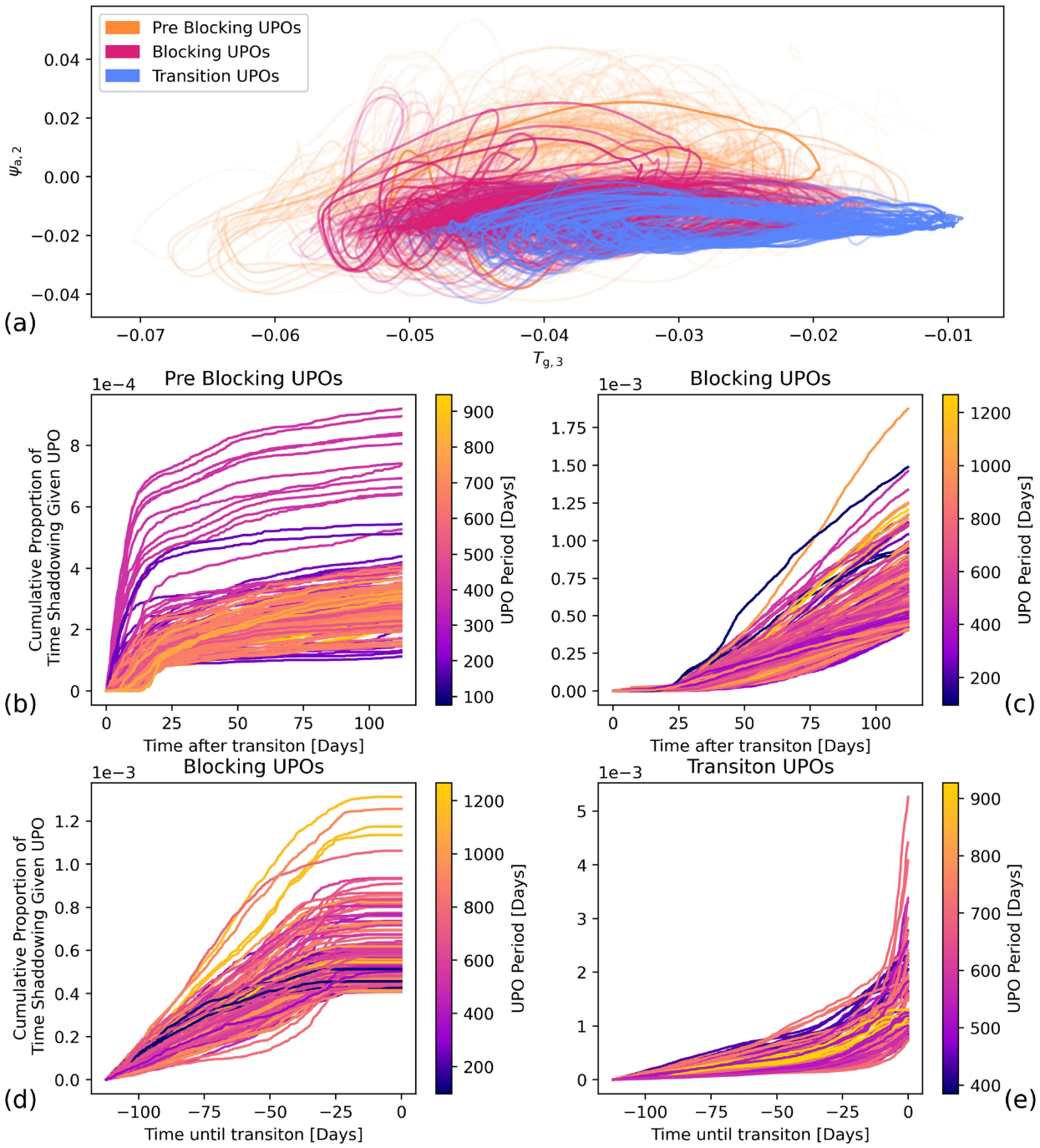


**FIG. 10.** Figure (a) shows the three sets of UPOs, color coded by which set they are in, the shade of the color displays the magnitude of CS overall, with darker shades representing UPOs that are shadowed more frequently. (b) Each curve represents a UPO, and the y axis shows the proportion of time that the UPO shadows the trajectory. The shading is the UPO period, showing that there is a wide range in the period of the UPOs shadowing the trajectory. This subplot shows the CS of the UPOs in the Pre-Blocking set [those in orange in (a)], for the first 100 days of the time in the cluster, where we see that the CS increases mainly in the first 25 days. Subplot (c) is for the same time period as (b), but showing the CS of the Blocking set of UPOs, shown in pink in (a). Here, we see that the CS increases relatively linearly after 25 days. Subplot (d) shows the CS of the set of Blocking UPOs for the final 100 days before transitioning. We see that the CS plateaus approximately 25 days before the transition. Finally, (e) shows the same as (d), but for the Transition set of UPOs, shown in blue in (a). Here, we see that the transition is captured by the exponential increase in the CS.

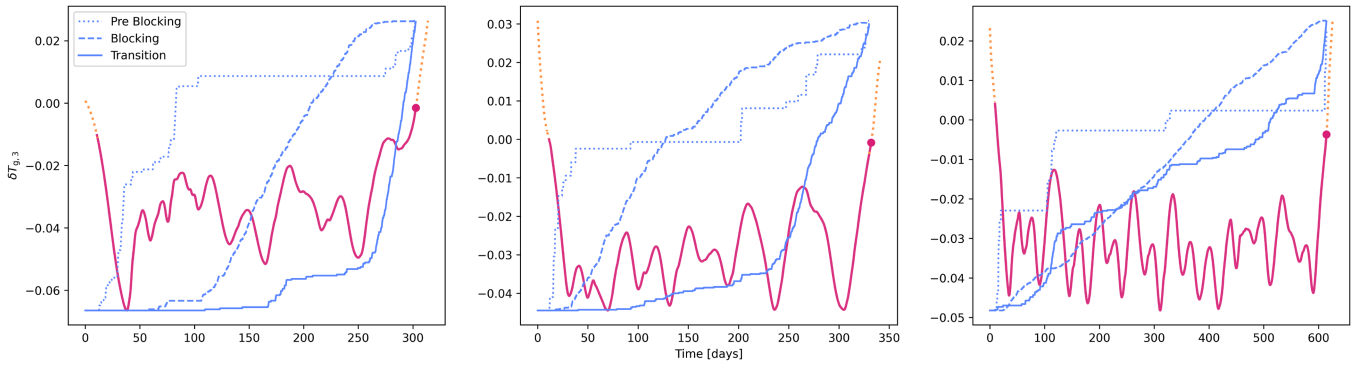


**FIG. 11.** Examples of CS of three trajectories in the left hand cluster. A time series of $\delta T_{g,3}$ is shown in pink when in the left hand cluster and orange when in the other cluster, a dot is shown where this transitions to the RHS cluster. The blue lines are the sum of the individual cumulative shadowing curves presented in Figs. 10(b)–10(e). The solid blue line shows the CS of the transition set, the dashed line shows the CS of the set associated with blocking, and the dotted line shows the CS of the pre-blocking set. We see before the transition the blocking set flattens out, while the CS of the transition set begins to increase considerably. All three CS curves are normalized and scaled for visualization purposes.

## IV. CONCLUSIONS

In this paper, identification of unstable periodic orbits and continuation methods were used to explain the dynamical behavior of a reduced order land–atmosphere model. While the use of UPOs to characterize atmospheric blocking has been studied before,[51,52] in both barotropic and baroclinic models, this study has built on this by using the UPOs to cluster the attractor into specific regions. These clusters were then used to identify transition regions and link these with atmospheric behavior.

The clusters in this model are of interest as they represent areas where the ground heat shows an anomaly in either the east or west regions of the domain. Through the heat transfers between the land and the atmosphere, this anomaly causes, on average, higher temperatures in the atmosphere, which can reinforce atmospheric blocking situations, which result from Rossby wave deflections induced by the orography.

This paper has also introduced a significant modification of the `qgs` framework,[23] which uses symbolic Python to construct the model equations. This modification allowed us to export the model equations in Julia (the language used for numerically finding the UPOs) and Fortran (formatted for using in the AUTO continuation software). In addition, it facilitated exporting certain parameter values as variables.

Through the use of continuation software, we have also been able to provide a more comprehensive understanding of the origin of the structure of the attractor that lead to atmospheric blocking. We found the paths to chaos from two stable orbits (for parameter values found in Xavier *et al.*[56]).

Finally, we explored the possibilities offered by the concept of shadowing of UPOs[46] to define cumulative shaddowing (CS) and identification of three sets of UPOs associated with different times of the blocking regime lifecycle. As the accuracy of numerical weather prediction's ability to forecast the onset and decay of atmospheric blocks still lags behind other features of the atmosphere, other methods that can forecast the onset or decay are of particular interest. While the approach that we used here is somewhat simplistic, we believe that proximity to particular UPOs or the rate of change of the CS could be useful as a training parameter in a machine learning, or more traditional forecasting approach, for forecasting transitions in state space.

Shadowing has been used with success in simple models to understand transitions,[47] and we believe that there is untapped potential to do similar for more complex models. In higher dimensional models, however, it could be more fruitful to analyze the shadowing of collections of UPOs rather than individual UPOs. This is because in higher dimensional systems, we will usually have fewer UPOs to study, and there are a larger number of unstable directions that the trajectory could diverge from the UPO.

Future work is required to investigate if similar techniques to those shown in this paper can expand to more complex models that more accurately model atmospheric blocking. In addition with the increase of global temperatures, and the change in north–south temperature gradients as a result of an anthropogenic climate change, such models and techniques could help understand how atmospheric blocking events will differ in the future, a topic that models and observations still differ largely on.[5,84]

## SUPPLEMENTARY MATERIAL

The supplementary material includes four sections, which provide some additional information and details to the main text. Section S-I provides additional details on the model used, as mentioned in Sec. II A, and includes additional projections of the model attractor. Section S-II describes the Newton–Raphson algorithm for finding the UPOs and the Tensor correction method. The convergence criteria used are also included in this section. Section S-III continues the bifurcation analysis for the right hand side cluster, as shown for the LHS in Sec. III C. Section S-IV provides information on the key shadowing UPOs for the RHS cluster, as done for the LHS in Sec. III F.

## ACKNOWLEDGMENTS

This project has received funding from the European Union's Horizon 2020 research and innovation program under Marie Sklodowska–Curie Grant Agreement No. 956170 (CriticalEarth). In addition, funding has been provided through the "Fédération Wallonie-Bruxelles" with the instrument "Fonds Spéciaux de Recherche." The authors would like to thank Anupama K. Xavier for providing results from previous studies, Professor Valerio Lucarini for discussions on periodic orbit theory, and Professor Dr. Ulrike Feudel for enlightening conversations on self-induced switchings between regimes. We also thank the two anonymous reviewers for their feedback on how to improve the original manuscript.

## AUTHOR DECLARATIONS

### Conflict of Interest

The authors have no conflicts to disclose.

### Author Contributions

**Oisín Hamilton:** Conceptualization (lead); Data curation (lead); Methodology (lead); Software (equal); Validation (equal); Visualization (lead); Writing – original draft (lead); Writing – review & editing (equal). **Jonathan Demaeyer:** Conceptualization (equal); Data curation (equal); Methodology (equal); Software (equal); Validation (equal); Writing – original draft (supporting); Writing – review & editing (equal). **Michel Crucifix:** Conceptualization (equal); Funding acquisition (equal); Methodology (equal); Supervision (equal); Validation (equal); Writing – original draft (supporting); Writing – review & editing (equal). **Stéphane Vannitsem:** Conceptualization (equal); Funding acquisition (equal); Methodology (equal); Supervision (equal); Validation (equal); Writing – original draft (supporting); Writing – review & editing (equal).

## DATA AVAILABILITY

The code used to numerically calculate the unstable periodic orbits can be accessed at https://github.com/ushham/Jupo.jl.[85] The bifurcation analysis was undertaken using the work of Demaeyer and Hamilton.[74] The qgs model framework v1.0 was developed by Demaeyer *et al.*[53] All repositories mentioned above are on GitHub.

## REFERENCES

[1] J. R. Holton, *An Introduction to Dynamic Meteorology* (Elsevier Academic Press, 2004), Vol. 88.
[2] J. Boyd, "Dynamical meteorology—Solitary waves," in *Encyclopedia of Atmospheric Sciences* (Elsevier, 2015), pp. 417–422.
[3] J. Ballester, M. Quijal-Zamorano, R. F. Méndez Turrubiates, F. Pegenaute, F. R. Herrmann, J. M. Robine, X. Basagaña, C. Tonne, J. M. Antó, and H. Achebak, "Heat-related mortality in Europe during the summer of 2022," Nat. Med. **29**, 1857–1866 (2023).
[4] R. Vautard, J. Cattiaux, T. Happé, J. Singh, R. Bonnet, C. Cassou, D. Coumou, F. D'Andrea, D. Faranda, E. Fischer, A. Ribes, S. Sippel, and P. Yiou, "Heat extremes in Western Europe increasing faster than simulated due to atmospheric circulation trends," Nat. Commun. **14**, 6803 (2023).
[5] P. Davini and F. D'Andrea, "From CMIP3 to CMIP6: Northern Hemisphere atmospheric blocking simulation in present and future climate," J. Clim. **33**, 10021–10038 (2020).
[6] A. Badza and G. Froyland, "Identifying the onset and decay of quasi-stationary families of almost-invariant sets with an application to atmospheric blocking events," Chaos **34**, 123153 (2024).
[7] M. C. Pinheiro, P. A. Ullrich, and R. Grotjahn, "Atmospheric blocking and intercomparison of objective detection methods: Flow field characteristics," Clim. Dyn. **53**, 4189–4216 (2019).
[8] S. Tibaldi and F. Molteni, *Atmospheric Blocking in Observation and Models* (Oxford University Press, 2018), Vol. 1.
[9] Intergovernmental Panel On Climate Change (IPCC), *Climate Change 2021—The Physical Science Basis: Working Group I Contribution to the Sixth Assessment Report of the Intergovernmental Panel on Climate Change* (Cambridge University Press, 2023).
[10] L.-A. Kautz, O. Martius, S. Pfahl, J. G. Pinto, A. M. Ramos, P. M. Sousa, and T. Woollings, "Atmospheric blocking and weather extremes over the Euro-Atlantic sector—A review," Weather Clim. Dyn. **3**, 305–336 (2022).
[11] E. Nabizadeh, P. Hassanzadeh, D. Yang, and E. A. Barnes, "Size of the atmospheric blocking events: Scaling law and response to climate change," Geophys. Res. Lett. **46**, 13488–13499, https://doi.org/10.1029/2019GL084863 (2019).
[12] T. Woollings, D. Barriopedro, J. Methven, S.-W. Son, O. Martius, B. Harvey, J. Sillmann, A. R. Lupo, and S. Seneviratne, "Blocking and its response to climate change," Curr. Clim. Change Rep. **4**, 287–300 (2018).
[13] T. A. Shaw, "Mechanisms of future predicted changes in the zonal mean mid-latitude circulation," Curr. Clim. Change Rep. **5**, 345–357 (2019).
[14] T. A. Shaw, M. Baldwin, E. A. Barnes, R. Caballero, C. I. Garfinkel, Y.-T. Hwang, C. Li, P. A. O'Gorman, G. Rivière, I. R. Simpson, and A. Voigt, "Storm track processes and the opposing influences of climate change," Nat. Geosci. **9**, 656–664 (2016).
[15] T. A. Shaw and A. Voigt, "Tug of war on summertime circulation between radiative forcing and sea surface warming," Nat. Geosci. **8**, 560–566 (2015).
[16] R. Vautard and B. Legras, "On the source of midlatitude low-frequency variability. Part II: Nonlinear equilibration of weather regimes," J. Atmos. Sci. **45**, 2845–2867 (1988).
[17] M. Mak, "A study of topographically induced multiple equilibria and low-frequency variability. I. Idealized topography," Q. J. R. Meteorol. Soc. **115**, 45–77 (1989).
[18] J. J. Nauw and H. A. Dijkstra, "The origin of low-frequency variability of double-gyre wind-driven flows," J. Mar. Res. **59**, 567–597 (2001).
[19] S. Vannitsem, J. Demaeyer, L. De Cruz, and M. Ghil, "Low-frequency variability and heat transport in a low-order nonlinear coupled ocean–atmosphere model," Phys. D: Nonlinear Phenom. **309**, 71–85 (2015).
[20] S. Vannitsem, J. Demaeyer, and M. Ghil, "Extratropical low-frequency variability with ENSO forcing: A reduced-order coupled model study," J. Adv. Model. Earth Syst. **13**, e2021MS002530 (2021).
[21] P. Maher, E. P. Gerber, B. Medeiros, T. M. Merlis, S. Sherwood, A. Sheshadri, A. H. Sobel, G. K. Vallis, A. Voigt, and P. Zurita-Gotor, "Model hierarchies for understanding atmospheric circulation," Rev. Geophys. **57**, 250–280, https://doi.org/10.1029/2018RG000607 (2019).
[22] D. A. Randall, R. A. Wood, S. Bony, R. Colman, T. Fichefet, J. Fyfe, V. Kattsov, A. Pitman, J. Shukla, J. Srinivasan, R. J. Stouffer, A. Sumi, K. E. Taylor, K. AchutaRao, R. Allan, A. Berger, H. Blatter, C. Bonfils, A. Boone, C. Bretherton, A. Broccoli, V. Brovkin, P. Dirmeyer, C. Doutriaux, H. Drange, A. Frei, A. Ganopolski, P. Gent, P. Gleckler, H. Goosse, R. Graham, J. M. Gregory, R. Gudgel, A. Hall, S. Hallegatte, H. Hasumi, A. Henderson-Sellers, H. Hendon, K. Hodges, M. Holland, A. A. M. Holtslag, E. Hunke, P. Huybrechts, W. Ingram, F. Joos, B. Kirtman, S. Klein, R. Koster, P. Kushner, J. Lanzante, M. Latif, T. Pavlova, R. Federationi, V. Petoukhov, T. Phillips, S. Power, S. Rahmstorf, S. C. B. Raper, H. Renssen, D. Rind, M. Roberts, A. Rosati, C. Schär, A. Schmittner, J. Scinocca, D. Seidov, A. G. Slater, J. Slingo, D. Smith, B. Soden, W. Stern, D. A. Stone, K. Sudo, T. Takemura, G. Tselioudis, M. Webb, M. Wild, E. Manzini, T. Matsuno, and B. McAvaney, "Climate models and their evaluation," in *Climate Change 2007: The Physical Science Basis. Contribution of Working Group I to the Fourth Assessment Report of the Intergovernmental Panel on Climate Change* (Cambridge University Press, 2007).
[23] J. Demaeyer, L. De Cruz, and S. Vannitsem, "Qgs: A flexible Python framework of reduced-order multiscale climate models," J. Open Source Softw. **5**, 2597 (2020).

[24]E. N. Lorenz, "The mechanics of vacillation," J. Atmos. Sci. **20**, 448–465 (1963).
[25]G. Veronis, "An analysis of wind-driven ocean circulation with a limited number of Fourier components," J. Atmos. Sci. **20**, 577–593 (1963).
[26]P. Cehelsky and K. K. Tung, "Theories of multiple equilibria and weather regimes—A critical reexamination. Part II: Baroclinic two-layer models," J. Atmos. Sci. **44**, 3282–3303 (1987).
[27]L. De Cruz, J. Demaeyer, and S. Vannitsem, "The modular arbitrary-order ocean-atmosphere model: MAOOAM v1.0," Geosci. Model. Dev. **9**, 2793–2808 (2016).
[28]J. G. Charney and J. G. DeVore, "Multiple flow equilibria in the atmosphere and blocking," J. Atmos. Sci. **36**, 1205–1216 (1979).
[29]J. G. Charney and D. M. Straus, "Form-drag instability, multiple equilibria and propagating planetary waves in baroclinic, orographically forced, planetary wave systems," J. Atmos. Sci. **37**, 1157–1176 (1980).
[30]B. B. Reinhold and R. T. Pierrehumbert, "Dynamics of weather regimes: Quasi-stationary waves and blocking," Mon. Weather Rev. **110**, 1105–1145 (1982).
[31]E. Kazantsev, "Unstable periodic orbits and attractor of the barotropic ocean model," Nonlinear Process. Geophys. **5**, 193–208 (1998).
[32]P. Cvitanović, R. Artuso, M. Mainieri, G. Tanner, and G. Vattay, *Chaos: Classical and Quantum* (ChaosBook.org, 2020).
[33]G. D. Birkhoff, "On the periodic motions of dynamical systems," Acta Math. **50**, 359–379 (1927).
[34]P. Cvitanović, "Invariant measurement of strange sets in terms of cycles," Phys. Rev. Lett. **61**, 2729–2732 (1988).
[35]C. Grebogi, E. Ott, and J. A. Yorke, "Unstable periodic orbits and the dimensions of multifractal chaotic attractors," Phys. Rev. A **37**, 1711–1724 (1988).
[36]J. L. Pughe-Sanford, S. Quinn, T. Balabanski, and R. O. Grigoriev, "Computing chaotic time-averages from a small number of periodic orbits," arXiv:2307.09626 (2023).
[37]D. L. Crane, R. L. Davidchack, and A. N. Gorban, "Minimal cover of high-dimensional chaotic attractors by embedded recurrent patterns," Commun. Nonlinear Sci. Numer. Simul. **140**, 108345 (2025).
[38]E. Sasaki, G. Kawahara, and J. Jiménez, "Bifurcation structure of unstable periodic orbits in plane Couette flow with the Smagorinsky model," Phys. Rev. Fluids **6**, 084608 (2021).
[39]G. J. Chandler and R. R. Kerswell, "Invariant recurrent solutions embedded in a turbulent two-dimensional Kolmogorov flow," J. Fluid Mech. **722**, 554–595 (2013).
[40]T. Kreilos and B. Eckhardt, "Periodic orbits near onset of chaos in plane Couette flow," Chaos **22**, 047505 (2012).
[41]G. Kawahara, S. Kida, and L. Van Veen, "Unstable periodic motion in turbulent flows," Nonlinear Process. Geophys. **13**, 499–507 (2006).
[42]G. Kawahara and S. Kida, "Periodic motion embedded in plane Couette turbulence: Regeneration cycle and burst," J. Fluid Mech. **449**, 291–300 (2001).
[43]S. Kato and M. Yamada, "Unstable periodic solutions embedded in a shell model turbulence," Phys. Rev. E **68**, 025302 (2003).
[44]B. R. Hunt and E. Ott, "Optimal periodic orbits of chaotic systems," Phys. Rev. Lett. **76**, 2254–2257 (1996).
[45]B. R. Hunt and E. Ott, "Optimal periodic orbits of chaotic systems occur at low period," Phys. Rev. E **54**, 328–337 (1996).
[46]C. C. Maiocchi, V. Lucarini, and A. Gritsun, "Decomposing the dynamics of the Lorenz 1963 model using unstable periodic orbits: Averages, transitions, and quasi-invariant sets," Chaos **32**, 033129 (2022).
[47]C. C. Maiocchi, V. Lucarini, A. Gritsun, and Y. Sato, "Heterogeneity of the attractor of the Lorenz '96 model: Lyapunov analysis, unstable periodic orbits, and shadowing properties," Phys. D: Nonlinear Phenom. **457**, 133970 (2024).
[48]F. M. Selten and G. Branstator, "Preferred regime transition routes and evidence for an unstable periodic orbit in a baroclinic model," J. Atmos. Sci. **61**, 2267–2282 (2004).
[49]A. Gritsun, "Statistical characteristics, circulation regimes and unstable periodic orbits of a barotropic atmospheric model," Philos. Trans. R. Soc. A **371**, 20120336 (2013).
[50]E. Kazantsev, "Sensitivity of the attractor of the barotropic ocean model to external influences: Approach by unstable periodic orbits," Nonlinear Process. Geophys. **8**, 281–300 (2001).
[51]A. S. Gritsun, "Unstable periodic trajectories of a barotropic model of the atmosphere," Russ. J. Numer. Anal. Math. Model. **23**, 345–367 (2008).
[52]V. Lucarini and A. Gritsun, "A new mathematical framework for atmospheric blocking events," Clim. Dyn. **54**, 575–598 (2019).
[53]J. Demaeyer, L. De Cruz, and O. Hamilton (2025). "Qgs," Version v1.0.0. Zenodo. https://doi.org/10.5281/ZENODO.15102613
[54]A. Meurer, C. P. Smith, M. Paprocki, O. Čertík, S. B. Kirpichev, M. Rocklin, A. Kumar, S. Ivanov, J. K. Moore, S. Singh, T. Rathnayake, S. Vig, B. E. Granger, R. P. Muller, F. Bonazzi, H. Gupta, S. Vats, F. Johansson, F. Pedregosa, M. J. Curry, A. R. Terrel, Š. Roučka, A. Saboo, I. Fernando, S. Kulal, R. Cimrman, and A. Scopatz, "SymPy: Symbolic computing in Python," PeerJ Comput. Sci. **3**, e103 (2017).
[55]D. Li, Y. He, J. Huang, L. Bi, and L. Ding, "Multiple equilibria in a land–atmosphere coupled system," J. Meteorol. Res. **32**, 950–973 (2018).
[56]A. K. Xavier, J. Demaeyer, and S. Vannitsem, "Variability and predictability of a reduced-order land–atmosphere coupled model," Earth Syst. Dyn. **15**(4), 893–912 (2024).
[57]M. Ghil, A. Groth, D. Kondrashov, and A. W. Robertson, "Extratropical sub-seasonal to seasonal oscillations and multiple regimes: The dynamical systems view," in *Sub-Seasonal to Seasonal Prediction* (Elsevier, 2019), pp. 119–142.
[58]P. V. Kuptsov and U. Parlitz, "Theory and computation of covariant Lyapunov vectors," J. Nonlinear Sci. **22**, 727–762 (2012).
[59]J. P. Eckmann and D. Ruelle, "Ergodic theory of chaos and strange attractors," Rev. Mod. Phys. **57**, 617–656 (1985).
[60]J. L. Kaplan and J. A. Yorke, "Chaotic behavior of multidimensional difference equations," in *Functional Differential Equations and Approximation of Fixed Points* (Springer, Berlin, 1979), Vol. 730, pp. 204–227.
[61]S. P. Kuznetsov, *Hyperbolic Chaos* (Springer, Berlin, 2012).
[62]E. J. Doedel and B. E. Oldeman, *Auto-07p: Continuation and Bifurcation Software* (Concordia University Canada, 2012).
[63]B. Mestel and I. Percival, "Newton method for highly unstable orbits," Phys. D: Nonlinear Phenom. **24**, 172–178 (1987).
[64]T. S. Parker and L. O. Chua, *Practical Numerical Algorithms for Chaotic Systems* (Springer, New York, 1989).
[65]S. C. Farantos, "Methods for locating periodic orbits in highly unstable systems," J. Mol. Struct.: Theochem **341**, 91–100 (1995).
[66]Y. Saiki, "Numerical detection of unstable periodic orbits in continuous-time dynamical systems with chaotic behaviors," Nonlinear Process. Geophys. **14**, 615–620 (2007).
[67]A. Abad, R. Barrio, and Á. Dena, "Computing periodic orbits with arbitrary precision," Phys. Rev. E **84**, 016701 (2011).
[68]R. Barrio, A. Dena, and W. Tucker, "A database of rigorous and high-precision periodic orbits of the Lorenz model," Comput. Phys. Commun. **194**, 76–83 (2015).
[69]A. S. Gritsun, "Unstable periodic orbits and sensitivity of the barotropic model of the atmosphere," Russ. J. Numer. Anal. Math. Model. **25**, 303–321 (2010).
[70]E. J. Kostelich, I. Kan, C. Grebogi, E. Ott, and J. A. Yorke, "Unstable dimension variability: A source of nonhyperbolicity in chaotic systems," Phys. D: Nonlinear Phenom. **109**, 81–90 (1997).
[71]J. J. Crofts and R. L. Davidchack, "On the use of stabilizing transformations for detecting unstable periodic orbits in high-dimensional flows," Chaos **19**, 033138 (2009).
[72]R. Veltz (2020). BifurcationKit.Jl. Inria Sophia-Antipolis, https://hal.science/hal-02902346.
[73]P. Clewley, W. Sherwood, M. LaMar, and J. Guckenheimer, "PyDSTool, a software environment for dynamical systems modeling," (2007); see http://pydstool.sourceforge.net.
[74]J. Demaeyer and O. Hamilton, "Climdyn/auto-AUTO: V0.5.1," Zenodo (2025); see https://doi.org/10.5281/zenodo.14901321.
[75]R. F. Pereira, S. E. De S. Pinto, R. L. Viana, S. R. Lopes, and C. Grebogi, "Periodic orbit analysis at the onset of the unstable dimension variability and at the blowout bifurcation," Chaos **17**, 023131 (2007).

[76]E. Barreto, B. R. Hunt, C. Grebogi, and J. A. Yorke, "From high dimensional chaos to stable periodic orbits: The structure of parameter space," Phys. Rev. Lett. **78**, 4561–4564 (1997).
[77]Y.-C. Lai, Y. Nagai, and C. Grebogi, "Characterization of the natural measure by unstable periodic orbits in chaotic attractors," Phys. Rev. Lett. **79**, 649–652 (1997).
[78]T. Grafke and E. Vanden-Eijnden, "Numerical computation of rare events via large deviation theory," Chaos **29**, 063118 (2019).
[79]G. Ansmann, K. Lehnertz, and U. Feudel, "Self-induced switchings between multiple space-time patterns on complex networks of excitable units," Phys. Rev. X **6**, 011030 (2016).
[80]G. Ansmann, R. Karnatak, K. Lehnertz, and U. Feudel, "Extreme events in excitable systems and mechanisms of their generation," Phys. Rev. E **88**, 052911 (2013).
[81]R. Karnatak, G. Ansmann, U. Feudel, and K. Lehnertz, "Route to extreme events in excitable systems," Phys. Rev. E **90**, 022917 (2014).
[82]E. G. Altmann, J. S. E. Portela, and T. Tél, "Leaking chaotic systems," Rev. Mod. Phys. **85**, 869–918 (2013).
[83]A. Ray, S. Rakshit, G. K. Basak, S. K. Dana, and D. Ghosh, "Understanding the origin of extreme events in El Niño southern oscillation," Phys. Rev. E **101**, 062210 (2020).
[84]J. Riboldi, F. Lott, F. D'Andrea, and G. Rivière, "On the linkage between Rossby wave phase speed, atmospheric blocking, and arctic amplification," Geophys. Res. Lett. **47**, e2020GL087796, https://doi.org/10.1029/2020GL087796 (2020).
[85]O. Hamilton (2025). "Jupo.jl—Newton-Raphson method for numerically finding unstable periodic orbits," GitHub. https://github.com/ushham/Jupo.jl.